Comparisons of Cloud In-Situ Microphysical Properties of Deep Convective Clouds to Appendix D/P using Data from the HAIC-HIWC and HIWC-RADAR I Flight Campaigns.

J. Walter Strapp[1], Alfons Schwarzenboeck[2], Kristopher Bedka[3], Thomas Bond[4], Alice Calmels[5], Julien Delanoë[6], Fabien Dezitter[5], Matthew Grzych[7], Steven Harrah[3], Alexei Korolev[8], Delphine Leroy[9], Lyle Lilie[10], Jeanne Mason[11], Rodney Potts[12], Alain Protat[12], Thomas Ratvasky[13], James T. Riley[14], and Mengistu Wolde[15]

[1] Met Analytics Inc., [2] Laboratoire de Météorologie Physique, U. Clermont Ferrand, [3] NASA Langley Research Center, [4] formerly Federal Aviation Administration, [5]Airbus Ind., [6] Laboratoire Atmosphères, Milieux, Observations Spatiales, [7] Boeing Commercial Airplanes, [8] Environment and Climate Change Canada, [9] formerly of Laboratoire de Météorologie Physique, [10] Science Engineering Associates, [11] U-ice LLC, [12] Australian Bureau of Meteorology, [13] NASA Glenn Research Center, [14] FAA William Hughes Technical Center, [15] National Research Council of Canada

Abstract

In-situ cloud data from three international flight campaigns are compared to the Federal Aviation Administration Title 14 Code of Federal Regulations Part 33 Appendix D mixed-phase/glaciated environmental envelope, and the corresponding identical European Aviation Safety Agency CS-25 Appendix P envelope. The appendices consist of a temperature-altitude envelope, a 99th percentile total water content envelope at the 17.4 Nm distance scale, a distance factor for estimation at other distance scales, ice crystal median mass diameter, and recommended liquid water content levels in mixed-phase icing conditions. The data were collected during 54 flights out of one subtropical and two tropical locations, with 472 runs from about 17,000' to 39,000' in approximately 115 clouds. The campaigns provide about 29,600 Nm of in situ data in deep convection over four targeted temperature intervals: -10, -30, -40, and -50, all ± 5 C. The dataset is a modern and unique documentation of the ice crystal icing environment, and results described in this article will contribute to regulatory and industry assessment of Appendices D and P.

Keywords: Ice crystal icing, Appendix D envelope, Appendix P envelope, deep convective cloud in-situ properties, engine power loss

1. Introduction

In 2014 and 2015, the Federal Aviation Administration (FAA) and the European Aviation Safety Agency (EASA) issued new aircraft certification rules [1, 2] that included the new and identical mixed-phase/glaciated environmental envelopes Appendix D and P respectively, hereafter referred to as Appendix D/P. The joint Engine Harmonization and Power Plant Installation Working Groups (EHWG/PPIHWG – hereafter the EHWG) and its successor the Engine Icing Working Group (EIWG) provided much of the substance of Appendix D/P [3], but acknowledged that the total water content (TWC) estimates were based on theoretical

calculations scaled to in-situ measurements from the 1950s [4], the latter from atmospheric temperatures warmer than about -26 C and with currently questioned accuracy. The liquid water content (LWC) levels in mixed-phase clouds were based on standards recommended by the British Joint Airworthiness Committee (JAC) [5], the origins of which were unclear. The ice particle median mass dimension range of 50-200 μm was based on limited flight data in high TWC clouds, which are now known to be subject to measurement artifacts in high ice water content (IWC) situations. For all the parameters above, there were very few adequately accurate modern alternative measurements which could have been used for an Appendix D/P assessment.

The EHWG thus identified the need for an instrumentation development effort followed by one or more flight campaigns to support atmospheric cloud characterization and Appendix D/P assessment. Campaign details and strategies were discussed and finalized in EHWG and EIWG discussions between 2004 and 2013. A series of flight campaigns were conducted, and in 2019 a new Aviation Rulemaking Advisory Committee (ARAC) commenced assessment of the appendix using the campaign results and other relevant information [6]. This article provides background on the development of Appendix D/P, and assembles a high level review of results from three flight campaigns conducted for its assessment, using new and existing material from published and unpublished reports, most notably [7-9] where more detail and supplementary material can often be found.

2. Background

As a result of the 1994 Avions de transport régional ATR-72 accident in Roselawn, Indiana [10, 11], the National Transportation Safety Board (NTSB) recommended expansion of the FAR 25 Appendix C icing certification envelope (hereafter Appendix C) "to include freezing drizzle/freezing rain and mixed water/ice crystal conditions, as necessary" [12]. As a consequence, the Ice Protection Harmonization Working Group (IPHWG) Aviation Rulemaking Advisory Committee (ARAC) was tasked to address NTSB recommendations, and established the joint Engine Harmonization and Power Plant Installation Working Groups (EHWG/PPIHWG hereinafter the EHWG) to examine the impact of Supercooled Large Drops (SLD)[1] and mixed phase/glaciated conditions on the certification rules for engines and power plant installations. The EHWG concluded that the dominant jet engine issue was power loss and/or engine damage in the vicinity of deep convective clouds, apparently related to ice crystals. A significant body of relevant information had been assembled in the 1950s, leading to standards recommended by the British JAC for ice crystal testing of aircraft engines and pitot probes [5], which are also the guidelines contained in the FAA Technical Document ADS-4 [15]. The recommendations can be traced to extensive flight campaigns in 1956-1958 by the Royal Aircraft Establishment (RAE) in the intertropical convergence zone, where TWCs up to 6.9 gm^{-3} over about 1.8 Nm were measured [4], mostly composed of ice crystals, and far in excess of Appendix C intermittent LWC maxima. British researchers at the time noted that a new form of icing had been discovered [16], dominated by high mass concentrations of ice crystals rather than supercooled LWC, one currently referred to as ice crystal icing (ICI).

The EHWG found no further reports of ICI until the 1990s, at which point aviation community knowledge of ICI had long been dormant. In the late 1990s, a commuter-class

[1] The American Glossary of Meteorology defines Supercooled Large Drops as those larger than 100 μm in diameter [13], consistent with the FAA Appendix O regulations for freezing drizzle and freezing rain [14].

aircraft experienced multiple engine rollback events near deep convective clouds [17]. The FAA issued a series of airworthiness directives limiting the flight envelope and requiring remedial modifications to the engines [18-22]. The industry investigation included a flight test campaign with an aircraft outfitted with a modified engine, during which an engine rollback in an unmodified engine was experienced in a cumulonimbus anvil composed of high TWC with little or no supercooled LWC [23, 24]. The studies of [17, 23, 24] provided the first contemporary evidence that engine icing could result primarily from ice crystals. In 2004, the EHWG assembled a database of approximately 100 engine events from 1990-2003 thought to be related to weather, where engine damage, compressor stall, power loss or roll-back had occurred, which led to a comprehensive update on the engine icing phenomenon [24]. Engine events, dominated by exposure to ice crystals, were now shown to be an industry wide problem observed over multiple aircraft and engine types, and distributed world-wide in geographical clusters. Meteorological analysis of the events highlighted that they occurred in the vicinity of thunderstorms but in otherwise seemingly innocuous cloud conditions. There were often no pilot-radar echoes, or at most green echoes (nominally $\leq$ 30 dBZ) in the immediate vicinity of the event. A total air temperature (TAT) anomaly was often observed [17, 23, 24], attributed to ingestion of ice crystals. A curious pilot observation of "rain on the windscreen" at seemingly impossibly cold temperatures in the absence of airframe icing and in low radar reflectivity was attributed to melting of ice crystals on the heated windscreen. Four events occurred at temperatures colder than -40 C, as have many more since. These studies led to the hypothesis that engine icing resulted from exposure to high ice crystal mass concentrations related to updraft regions of deep convective clouds, and that atmospheric supercooled LWC was not required. Furthermore, low radar reflectivity suggested that the ice particles were relatively small [24]. Since the meetings of the EHWG, it has been shown that ICI can also adversely affect airspeed measurements from pitot probes [25].

In 2007, the EHWG published the interim Appendix D/P envelope [3]. The temperature-altitude envelope extended Appendix C boundaries to encompass the engine event database. For TWC, some conventions of Appendix C were adopted, namely the choice of a 99th percentile water content and a reference distance of 17.4 Nm. Theoretical calculations of maximum condensed "adiabatic" water content, assuming deep lift from the boundary layer, were down-scaled to 65% to equal the 99th percentile TWC (TWC_{99}) at the 17.4 Nm distance scale calculated from the 1950s RAE dataset [4] ,the only sufficiently large dataset available at the time. The TWC distance factor relative to 17.4 Nm was also computed from the same RAE dataset. Information on the levels of LWC in high TWC clouds was very limited. No quantitative information was available from the 1950s RAE dataset, and only sparse information was available from atmospheric science community measurements. Consequently the existing FAA ADDS-4 LWC level guidelines [15] were adopted for Appendix D/P. These can be traced back to the 1958 British JAC recommendations, reported shortly after the RAE had completed its 1950s flight campaign measurements in which LWC measurements were not provided. It appears that the JAC LWC recommendations were not derived from Appendix C or the similar British Civil Transport design criteria, but were best estimates based on other available knowledge, and simply cited as "reasonable for design purposes" [5]. Information on particle size in high IWC conditions was likewise limited, although particles were suspected to be relatively small. Results from the commuter-class rollback aircraft flight trials [23], and from hurricane flights [26] were used to estimate the Appendix D/P ice crystal size median mass dimension range of 50-200 μm, although both studies cited considerable uncertainty due to

poorly understood instrument performance in high IWC conditions. These estimates were to some degree supported by the Airbus A340 flight test measurements noted below, but the measurements of [23] and [26] are now known to be subject to ice crystal shattering artifacts [27], biasing the median sizes low. Results from the current flight campaigns arguably provide the first reliable extensive TWC measurements, mixed-phase LWC levels and particle size measurements of the ICI environment.

During the period of 2010-2012, while plans were underway to conduct the first of the three campaigns providing data for this article, Airbus Ind. performed a series of exploratory flight test campaigns in Darwin, Cayenne, and Chile with their A340 test aircraft [28]. These campaigns provided important preliminary information on the TWC levels that could be expected in deep convective clouds, up to an estimated 5.5 gm^{-3} over short distance scales, and confirmed that high TWC could be encountered in cloud regions commercial pilots would routinely traverse. The campaign also occasionally experienced "rain on the windscreen" in ice crystal conditions, confirming the ice crystal windscreen melting hypothesis of [24]. This observation has subsequently been confirmed in all of the flight campaigns noted in this article.

Due to the uncertainties in the envelope, FAA and EASA agreed to review the results of new measurements within the newly formed ICI ARAC to identify any appropriate modifications to Appendix D/P, using information from the flight campaigns and any other relevant information. The deliberations of that committee are ongoing.

3. Flight Campaigns

The EHWG recommended a dedicated flight campaign with modern and improved instrumentation to provide data to assess Appendix D/P. Data from three flight campaigns are used for the analysis of this article. The first two were accomplished as part of an international effort between the European High Altitude Ice Crystals (HAIC; [29]) and North American HIWC [30] projects. The first HAIC-HIWC campaign was conducted from 16 Jan. to 18 Feb. 2014 in Darwin, Australia (hereafter Darwin-14) using the Service des Avions Français Instrumentés pour la Recherche en Environnement (SAFIRE) Falcon-20 cloud research aircraft. The second was conducted from 5-29 May 2015 in Cayenne, French Guiana (hereafter Cayenne-15) to collect additional data, where the Falcon-20 was joined by the National Research Council (NRC) of Canada Convair 580 aircraft, also equipped for cloud in-situ measurements. The third, the National Aeronautics and Space Administration (NASA) /FAA HIWC-RADAR I campaign [31], was conducted from 12-29 Aug. 2015 out of Fort Lauderdale, Florida (hereafter Florida-15) with a NASA DC-8 aircraft. Flight tracks from the three campaigns are shown in Figures 1-4. The flight campaigns were conducted by scientists and engineers from the international atmospheric science and aviation communities highly experienced in making airborne cloud measurements.

In all flight campaigns, the research aircraft were outfitted with the same core instruments (section 4), to make in-situ measurements of cloud TWC and particle size distributions (PSDs) to support the comparisons to Appendix D/P. Geographical locations and time periods were chosen to optimize measurement of large oceanic mesoscale convective systems (MCS) known to be associated with the majority of engine events (section 5). Since at the outset it was unknown how extreme conditions would be, and whether, for example, an engine power loss would be experienced, safety and local airport facilities were also of primary concern. Other major considerations included the existence of local weather measurements and forecasting, air traffic density, and the cooperation of Air Traffic Control for freedom of flight. Darwin is located near

the Pacific Ocean Tropical Warm Pool, the region of the highest sea surface temperatures in the world, which fuel deep convection and potentially high cloud water contents. This region experiences a high frequency of MCSs during the monsoon season, with some of the deepest oceanic convection globally. It possesses good operational ground-based radar and lightning networks, excellent airport facilities, a regional weather forecasting office, and at the time, the world's most extensive tropical ground-based cloud remote sensing facilities. Satellite images, which provide crucial storm structure and evolution information, and which have been used heavily in past engine event analyses, were provided for this project by the Japan Meteorological Agency (JMA) at a 10 minute frequency, rather than the usual 60 minutes available in Australia at the time. Upon completion of Darwin-14, the project's data collection goals had not been fully met. It was then decided to conduct a second campaign, taking advantage of the opportunity to collect data at a second location. In May, French Guiana experiences a similar climatological frequency of oceanic deep convection as Darwin's monsoon season, some of which was expected to be associated with the Atlantic Intertropical Convergence Zone (ITCZ). Cayenne offered good meteorological and ground-based logistical support and freedom of flight. Finally, Florida-2015 was conducted to test pilot radar high IWC detection algorithms, with the secondary objective to collect the final missing data for the Appendix D/P comparison, particularly those at the higher altitudes. In addition to MCS sampling in the Gulf of Mexico and off the southeastern US coast, convective cells were sampled in four flights in two tropical storms over the Caribbean Sea. Although the frequency of engine events in tropical storms has not been specifically estimated to date, three of eleven Boeing case studies of oceanic southeast Asian events were associated with such storms [32]. Tropical storms persist for days, and provide a fertile environment for efficient data collection. The use of the DC-8 in Florida-2015 enabled transit to more distant targets, and longer sampling at high altitude. These three locations all provided data in warm tropical oceanic atmospheres, which will be shown in section 6.1 to be similar to the majority of engine events. However, as elaborated in section 7, they may not fully represent deep convective cloud conditions expected to be encountered globally by commercial aviation.

.

4. Cloud Instrumentation

Full lists of campaign instruments have been provided for the Falcon-20 [7], Convair 580 [33], and DC-8 [31]. Each aircraft carried a common set of core cloud instruments described below, which has been used to provide the Appendix D/P comparison dataset. The EHWG recognized issues in measuring the harsh high-TWC environment, and recommended instrument testing, evaluation, and development prior to the new flight campaigns. A major instrument effort was undertaken between 2006 and 2013. Activities included the development of a new reference TWC probe, modifications to probes to minimize artifacts in PSD measurements and to reduce probe sensitivity to electrostatic charging, increases to probe de-icing, and various other improvements. A more detailed list of efforts of the HIWC team has been provided in [30].

The measurement of TWC was of particular importance for the flight campaigns. The EHWG reviewed the methods available in 2006, and concluded that a new instrument was required due to poorly defined accuracy and reliability of existing methods in high-TWC conditions. A new TWC instrument was proposed, specifically designed to measure of up to 10 gm^{-3} at 200 ms^{-1} and 200 kPa with an accuracy of 20%, adapting an existing inlet-based

evaporator technique that used differential hygrometry for TWC estimation. Baumgardner et al. [34] summarizes similar earlier devices. Details on the activities of the HIWC team related to the development, performance evaluations and accuracy estimation of the prototype and final Isokinetic Probe (IKP2) have been detailed elsewhere [35-41]. Due to increasing levels of background water vapor (BWV) as temperatures increase, the use of the probe in turbulent tropical environment was practically limited to temperatures colder than about 0 C [41]. Although somewhat difficult to quantify due to the lack of accurate IWC test facilities and reference standards that could accommodate the IKP2, it is contended that the design accuracy of 20% was met and likely exceeded, particularly for the high 17.4 Nm distance scale TWC_{99} values derived from the flight campaign datasets. The IKP2 probe was mounted under the wing of each aircraft, as illustrated in Figure 5 for the Falcon-20 and Figure 7 for the DC-8.. Two copies were manufactured, for simultaneous use on both the Falcon-20 and Convair 580 during the Cayenne-15 campaign. The probes performed well during the three campaigns.

In addition to the IKP2, the Science Engineering Associates (SEA) Robust hot-wire probe (Fig. 5) provided secondary estimates of TWC on each of the aircraft. The Robust probe is a hot-wire TWC probe enhanced by SEA for durability in the harsh high-TWC environment, and was initially used for estimation of IWC profiles in the NRC M7 test cell [42]. It was also used during the Airbus A340 exploratory flights in high TWC [28]. The Robust IWC efficiency was initially not well characterized, and estimated to be about 0.4. As a result of comparisons to the IKP2 flight campaign data, understanding of the IWC efficiency has greatly improved, although remains uncertain for IWCs greater than about 3 gm^{-3} [7]. The Robust probe provided valuable qualitative corroboration of the IKP2 time-history data for the current study, and was occasionally used as a surrogate to fill IKP2 data gaps. Its use in mixed-phase conditions however is not straightforward due to differing IWC and LWC collection efficiencies.

The core airborne instruments used for the PSD and Median Mass Diameter (MMD) measurements were the Droplet Measurement Technologies (DMT) Cloud Droplet Probe [43] version 2 (CDP-2, 2-50 μm), the Stratton Park Engineering Co.(SPEC) 2D-Stereo Probe (2D-S, nominally 10-1280 μm) [44], and the DMT Precipitation Imaging Probe (PIP, nominally 100-6400 μm). The 2D-S and PIP are imaging spectrometers that require complex analyses to retrieve PSDs and MMD, as described for this project in [45]. These three probes were mounted under the wings of each campaign aircraft. Prior to the campaigns, Environment and Climate Change Canada (ECCC) undertook an extensive program to improve PSD measurements by reducing errors created by debris from ice crystal shattering and bouncing from upstream probe surfaces [46-48, 27], errors known to be present in the interim Appendix D/P particle size guidelines. The efforts included improvement of ice crystal image analysis algorithms, and modifications to probe housings to mitigate shattering and/or deflect debris away from the active sample volume [49-51]. The CDP-2 is a version of the CDP modified by ECCC and the manufacturer for this purpose. The SPEC 2D-S probes also incorporated the most recently available probe tips provided by the manufacturer for mitigation of shattering debris. The CDP-2, 2D-S, and PIP were installed under the wings of each campaign aircraft, as illustrated for the DC-8 during the HIWC RADAR I campaign in Figures 6 and 7. The core PSD instrumentation applied the most up to date airborne technology and software algorithms in common use in the atmospheric science community.

The measurement of the observed low-LWC mixed-phase levels in the ICI environment is challenging [52]. The primary instruments were the Rosemount or Goodrich Icing Detectors [53], the DMT CDP2, images from the various spectrometers, and additionally for the Convair

580, a modified Particle Measuring Systems Forward Scattering Spectrometer Probe (FSSP-100), and a Nevzorov LWC/TWC hot-wire probe [54].

5. Target Cloud Systems, Flight Plans, and Data Collection Summary

Strategies for campaign data collection were developed by the EHWG and EIWG between 2006 and 2013, and have been summarized in [30]. The campaigns targeted the primary engine-event cloud type [22, 52-53], the tropical oceanic MCS with a nominal characteristic size of 100 Nm or greater. A secondary target was isolated afternoon continental convection, expected to be more vigorous than oceanic convection. Convectively active cells were directly sampled in the more benign systems, or from a safe distance in the more vigorous systems. The basic reference TWC statistic was TWC_{99} at the 17.4 Nm distance scale. An EIWG analysis of the 1950s RAE data by an industry statistician estimated that at least 100 data points at 17.4 Nm would be required to define TWC_{99} with a ±20% sampling accuracy. After a post-Darwin-14 adjustment, the EIWG requested that at least 100 17.4 Nm data points be collected within the following 4 temperature intervals, in order of priority: -50 ±5 C, -40 ±5 C, -30 ±5 C, and -10 ±5 C.

A breakdown by distance of the data collection for major cloud types is shown in Figure 8. About 93% of the in-cloud data were collected in MCS of tropical oceanic origin, including six flights in tropical storms. About 7% of the data were collected in afternoon continental systems driven by the solar cycle. These proportions were similar to the 85% and 15% suggested by the EIWG. Table 1 shows general characteristics of the large MCS sampled during the campaigns, and some comparisons to available engine event cloud characteristics. The first row compares cloud sizes from the three campaigns, as arbitrarily defined from the area of satellite infrared (IR) pixels at or colder than -50 C. Clouds were largest in Darwin-14 (median 210 Nm area equivalent diameter), followed by Florida-15 (160 Nm), and Cayenne-15 (100 Nm^2). Engine event studies [32, 55-58] identified the "enhanced distance", the length an event-aircraft traversed under cloud tops colder than the approximate tropopause temperature or convective equilibrium level, as a potentially important metric for engine ICI susceptibility. The studies of [32, 57] showed that the median enhanced distances of 130 and 137 Nm for 52 global and 11 oceanic southeast Asia events respectively were a little larger than the 105 Nm for Darwin-14 (Table 1, row 2). Minimum event cloud top IR temperatures in southeast Asia were similar to Darwin-14 (medians of -84 and -80 C respectively) while the median global event IR temperature (-63 C) was more similar to median Cayenne-15 (-62 C) and Florida-15 (-61 C) values (row 3). Thus it can be argued that the three campaign locations combined to represent both the colder topped engine-event clouds of oceanic southeast Asia and Australia, and the warmer global medians. Atmospheric precipitable water, an estimate of the total depth of water vapor in a column of the atmosphere if condensed to liquid (row 4), was highest in Darwin-14 with a median of 60 mm, and lowest in Florida-15 at 51 mm. The global median for engine events was 58 mm [57], and 64 mm for 11 engine events in oceanic southeast Asia [32].

Based on engine events, flight tracks were ideally restricted to traverse the region encompassing active cells, and pass within about 20 Nm of any heavy rain area identifiable below the aircraft. A typical flight track in an un-named tropical storm near Darwin is shown in

[2] Afternoon continental cumulonimbus anvils were sampled only in Cayenne-15, and had a corresponding median size of 55 Nm. They were excluded in the data used to calculate the Cayenne-15 100 Nm characteristic size in Table 1.

Figure 9, along with time histories in Figure 10 of selected parameters for one traverse. The background for this figure is a Japanese Multifunctional Transport Satellites (MTSAT) IR satellite image, where cloud top temperatures at or colder than -78 C are shown in white to purple colors (see legend). Project scientists on the ground typically suggested coordinates for a first traverse across the cloud system. The pilot and on-board scientists were free to modify the track to optimize expected exposure to high TWC using tilt and maximum gain on the pilot's radar, while maintaining normal commercial flight distances from any red echo regions. Subsequent traverses were chosen to attempt a survey pattern around the most convectively active areas. In Figure 10, the cloud top above the aircraft reached about -85 C and 55,500' pressure altitude, and TWC at the average flight altitude of 33960' reached about 3.5 gm^{-3}. The aircraft passed through an updraft region reaching about 18 ms^{-1}, roughly co-located with the highest TWC measurements.

Overall, the three campaigns provided 54 flights in one sub-tropical and two tropical locations, with 472 traverses in approximately 115 clouds from about 17,000' to 39,000' in pressure altitude, providing about 29,600 Nm of in-cloud data in deep convection over the four targeted temperature intervals. Cloud traverse lengths were similar in all campaigns, with average and maximum values of 63 and 236 Nm. Campaign traverse-average TWCs were also similar, with an overall average of 0.70 gm^{-3}.

TWC data were transformed to distance coordinates, and then analyzed to provide data points averaged over the following 13 arbitrarily chosen distance scales: 0.5, 1, 2, 5, 10, 15, 17.4, 20, 30, 40, 50, 75, and 100 Nm. To be compatible with Appendix D/P, the data points were back-to-back and non-overlapping, starting at the first continuous exceedance of 0.1 gm^{-3} from the cloud edge. This was not the only option for defining data points, and other definitions may be explored in future analyses. The current data point definition, when compiled over the collection of clouds, roughly provided a frequency distribution of the grid space of in-cloud TWC over the area domain of the flight tracks. Each cloud traverse provided multiple data points to the dataset, and each traverse of each cloud was included. There were naturally more short distance scale points than long, roughly scalable by the ratio of the distance scale. Table 2 displays the number of 17.4 Nm data points collected. The unrequested -20 C interval is shown here solely to demonstrate the lack of data points, and will not be discussed further. Due to a variety of circumstances, most of the -10 C and -50 C data were collected in Cayenne-15 and Florida-15 respectively, while -30 and -40 C data collection was more evenly distributed. In all targeted intervals, the requested 100 points at 17.4 Nm was sometimes exceeded in single subsets, and comfortably exceeded in the composite set.

6. Results and Comparisons to Appendix D/P

6.1. Temperature-Altitude Envelope

An analysis was performed to determine if the temperature-altitude environment of the flight campaign data was similar to engine events. Figure 11a shows most recent record of Boeing engine events overlaid on the Appendix D/P temperature-altitude envelope [58]. Figure 11b shows the average temperature versus pressure altitude for each traverse of the three flight campaigns. Average radiosonde profiles for the three campaign periods are shown as solid lines. Although the two figures reveal similar distributions, engine-event points are spread somewhat broader, reflecting their wider seasonal coverage, while the warm season flight campaign points surround their average radiosonde profiles and thus the warmer region of the Appendix D/P

envelope. The flight campaign measurements also do not extend to the near -60 C reached by engine events, because the coldest campaign targeted temperature interval was -50 C.

6.2. Occurrence of Mixed-Phase and LWC Levels.

The identification and characterization of mixed-phase regions in high-IWC clouds with low LWC, such as those encountered in the flight campaign data, is challenging due to limitations of the cloud instrumentation [52]. The strategy used here, described in [59] and similar to that of [60], was to apply accumulated experience and the best practical combination of instruments to estimate the occurrence and levels of LWC. Possible mixed-phase zones were signaled by elevated CDP-2 and/or FSSP concentrations greater than 10 cm^{-3}, after which spectral overlap with the 2D-S was examined to eliminate false positives due to shattering artifacts. A second more definitive identifying signal was a decrease in the vibration frequency of the Goodrich ice detector, indicative of ice accretion. LWC levels in mixed-phase zones identified this way were estimated from ice detector ice accretion rates, FSSP-100 or CDP-2 integrated LWC, and/or Nevzorov hot-wire estimates, depending on the dataset and the situation. The minimum detectable LWC threshold was of the order of 0.01 gm^{-3}, due to the various limitations of these instruments. The fine points of the results might be expected to vary according to the particular analyst and combination of instruments, but the important mixed-phase conclusions are clear and consistent. Cloud TWC was highly dominated by ice crystals, mixed-phase zones were rare, and when encountered, LWC was low. Mixed-phase was usually on the edges or in between large ice clouds, and was only occasionally imbedded in broad high-IWC zones. Mixed-phase statistics, summarized in Table 3, were estimated only for the Darwin-14 and Cayenne-15 data. The ice detector was only recorded for the last four flights of Florida-15, during which no mixed-phase zones were observed. It was estimated from Convair 580 data that the spatial fraction of mixed-phase in the -10 C interval with LWC greater than or equal to 0.1 gm^{-3} was only about 5%, with average LWC never exceeding about 0.25 gm^{-3}. The horizontal extent of such zones was usually less than a few nautical miles. From the Falcon-20 data, the spatial fraction at -10 C was a similar 2.8%, with a maximum zone-average LWC of 0.32 gm^{-3}, and a maximum exposure distance of 7.9 Nm (medians of 0.08 gm^{-3} and 1.8 Nm respectively). The spatial fraction decreased with decreasing temperature as expected, to about 0.2% in the -30 C interval. There were no mixed-phase zones colder than -35 C.

There are some notable differences between the campaign observations and the "Supercooled Liquid Portion of TWC" provided in Appendix D/P (Table 4). While the Appendix identifies no LWC for temperatures colder than -20 C, the flight campaign measured traces of LWC to -35 C. Furthermore, while Appendix D/P indicates the upper LWC bounds of 1.0 gm^{-3} for less than 50 Nm, and 0.5 gm^{-3} over indefinite length scales, the flight campaign LWC levels were considerably lower and the zones were much narrower. As discussed in section 2, Appendix D/P mixed-phase guidelines do not appear to have been derived from any specific measurements, but were simply defined in 1959 as reasonable for design purposes. In regards to the flight campaign clouds, it is important to note that they were mostly large oceanic MCS sampled in their mature stages, had tops typically colder than -60 C, and widespread areas of high ice concentrations that could mix to lower altitudes and grow at the expense of the liquid content of any imbedded updraft. They were also flown in a manner consistent with commercial aviation, avoiding, when present, areas of excessive lightning and radar red-echo at altitude where LWC may have more likely been found. A survey of the atmospheric science literature did not reveal any comprehensive description of the mixed-phase properties of large deep

convective clouds. In limited measurements of large tropical MCS and hurricanes, less extensive than the measurements of this study, LWC was only found in active cells, and mainly at temperatures warmer than about -12 C [61, 62]. Large stratiform regions of MCS that composed most of the cloud area were glaciated [61, 63], as in the current study. There is however some evidence that continental convection may have a higher LWC potential due to postulated differences in the rates at which glaciating ice particles are formed in updrafts [64]. Relatively narrow updrafts of continental towering cumulus and thunderstorm feeder cells can contain substantial LWC to -30 C and colder, particularly in cells that had not yet grown above the -40 C level [64, 65]. The most extreme dataset in this regard [64] contained high LWC in mixed-phase to -38 C in continental MCS feeder cells about 0.8 to 6 Nm wide. In one example with an out-of-cloud temperature of about -31 C, a 1.4 Nm wide cell had sustained LWC greater than 2 gm^{-3} and a peak of about 3.8 gm^{-3}.

These overall observations indicate that the regions of large oceanic MCS likely to be traversed by commercial aviation can contain imbedded mixed-phase cells to temperatures colder than -30 C, but typically with length scales less than about 8 Nm, and with average LWC likely less than a few tenths of a gm^{-3}. In both oceanic and continental MCS, there is no evidence that LWC levels can be sustained over indefinite length scales, particularly at typical commercial aviation flight altitudes. There may be more substantial intermittent LWC in continental clouds, and in the extreme case, narrow updrafts may reach several gm^{-3}, particularly in new growing cells surrounding or attached to the mature MCS. In this regard, it may be prudent to assume that the mixed-phase results of the three flight campaigns are specific, and may not extend to continental deep convection, and/or smaller clouds that have not reached the -40 C level, and that the venerable Appendix C intermittent maxima may better encompass general deep convective mixed-phase conditions until more comprehensive information becomes available.

6.3. Maximum TWC Values

Campaign maximum TWCs averaged over distance scales from 0.5-100 Nm are displayed in Figures 12(a-d) for the -50, -40, -30, and -10 C intervals respectively. In each figure, the Darwin-14, Cayenne-15 Falcon-20, Cayenne-15 Convair 580 (-10 C only), and Florida-15 data are shown as blue, red, purple, and green symbols respectively. Differences between these data subsets will be discussed in section 7. The overall maximum at each distance scale is circled in light grey. The maxima decreased with the distance scale as expected due to distance averaging. At 0.5 Nm, the overall maxima in the four temperature intervals from -50 to -10 C were 2.7, 3.6, 4.1, and 4.0 gm^{-3} respectively, from the Falcon-20 in Cayenne-15 in each case, reaching between 54% to 72% of the distance-factor adjusted Appendix D/P values. At the 17.4 Nm distance scale, the corresponding maxima decreased to 2.0, 2.8, 2.7, and 3.0 gm^{-3}, contributed by Florida-15, Darwin-14, and Cayenne-15 (Falcon-20) respectively, between 54 and 67% of Appendix D/P. Even at the 100 Nm distance scale, overall maxima were near 2 gm^{-3} in the -10 and -30 C intervals.

6.4. Ninety-Ninth Percentile TWC Values

The corresponding TWC_{99} values versus distance scale are displayed in Figures 13 (a-d). Processing of TWC_{99} values is discussed in detail in [9, 41, 67]. TWC_{99} values were estimated using a simple ranking procedure described as method 7 in [66]. Since this method sets the

maximum dataset value to the 100th percentile, low-bias and uncertainty was expected in TWC_{99} due to the finite sample size. Furthermore, additional bias and uncertainty was expected due to the assumption of ice saturation BWV in the IKP2 calculation. The combined bias and sample uncertainty due to these influences was estimated using a Monte Carlo procedure that produced a synthetic IKP2 campaign data set with noise and bias randomly injected for BWV uncertainty, which was then re-sampled repeatedly with replacement using a bootstrap procedure to estimate final bias and uncertainty. Uncorrected TWC_{99} values are shown in Figures 13 (a-d) as open symbols, with the bias-corrected values as the small solid circles of the same color, usually imbedded within the open symbol because the bias corrections are minor. Due to the significant data point overlap, an artificial offset was applied to the distance scales for each dataset for better visualization. Open symbols were plotted only for points with greater than or equal to 100 samples, but bias-corrected values with $\pm 2\sigma$ uncertainty bars were arbitrarily extended one additional distance scale. Campaign TWC_{99} percentages of the appendix at 17.4 Nm are listed in the inset text boxes, with arrowed lines pointing to the data points used to calculate the percentages.

In the highest priority -50 C temperature interval (Fig. 13a), the majority of data were collected during Florida-15 (Table 2). The TWC_{99} versus distance curves from the three locations were very similar. Combining all datasets, the composite TWC_{99} value at 17.4 Nm was 1.84 ± 0.14 gm^{-3} ($\pm 2\sigma$), about $50.1 \pm 3.8\%$ of the Appendix D/P value of 3.68 gm^{-3}. More than 100 composite data points were available to the 30 Nm distance scale, at which the TWC_{99} value decreased to 1.75 gm^{-3}. In the -40 C interval (Fig. 13b), the Darwin-14 and Cayenne-15 curves were similar, but Florida-15 TWC_{99} values were significantly lower, particularly at the shorter distance scales. The number of data points provided from each location was similar, and there is no obvious explanation for this difference given the similarity at -50 C. The composite TWC_{99} value at 17.4 Nm increased from that at -50 C to 2.14 ± 0.25 gm^{-3}, about $53.7 \pm 6.2\%$ of the Appendix D/P value of 3.98 gm^{-3}. The longest distance scale with 100 points was 50 Nm, where the TWC_{99} value was again 1.75 gm^{-3}. In the -30 C interval (Fig. 13c), the TWC_{99} values from the 3 locations, with similar contributions of data points, were similar. The composite TWC_{99} value at 17.4 Nm again increased to 2.34 ± 0.19 gm^{-3}, $53.8 \pm 4.4\%$ of the Appendix D/P value of 4.35 gm^{-3}. One hundred composite data points were available to 50 Nm, where TWC_{99} was 2.16 gm^{-3}. Finally, in the -10 C interval (Fig. 13d), 94% of the 17.4 Nm data points were from Cayenne-15 (Falcon-20 and Convair-580). There were significant differences between the four datasets at -10 C, although data points from Darwin-14 and Florida-15 may simply be too few to be meaningful. The same cannot be said for the difference between the Falcon-20 and Convair-580 in Cayenne-15, which is discussed in section 7. The 17.4 Nm composite TWC_{99} value again increased, to 2.66 ± 0.27 gm^{-3}, $58.8 \pm 5.9\%$ of the Appendix D/P value of 4.52 gm^{-3}. One hundred data points were collected to 30 Nm, where the TWC_{99} value was 2.61 gm^{-3}.

The composite TWC_{99} results were significantly lower than Appendix D/P values at all distance scales. At the 17.4 Nm reference scale, TWC_{99} increased with temperature (decreased with altitude) at roughly the same rate as Appendix D/P, as shown in Figure 14. Values varied between about 50 and 59% of Appendix D/P, or roughly half of the appendix. The correlation with altitude provides some support for the application of adiabatic water content estimates as a physical basis for establishing Appendix D/P levels in these deep tropical oceanic clouds, at least for the warm tropical atmospheres of the campaigns. If the datasets of this study had been used by [3] to establish the factor for empirically downscaling adiabatic TWCs for the Appendix D/P

17.4 Nm reference distance, the scale factor would have been about 0.36, rather than the 0.65 calculated by [3] from the 1950s RAE dataset.

Figure 15 alternatively shows the flight campaign 17.4 Nm TWC_{99} values overlaid on the Appendix D/P TWC envelope. The four red open circles show the campaign values for the 4 temperature intervals, each 10 C wide. The symbols are plotted at the average temperatures and pressure altitudes of the data points in the interval. The corresponding Appendix D/P values are identified directly above as open circles at the color closest to the original Appendix D/P temperature curves. A vertical arrow identifies the pairs for comparison, and as already illustrated in Figures 13 and 14, campaign values were about a factor of two lower. Clearly, only the warmer sector of the Appendix has been assessed, with no data points in the colder winter convective cloud corner at the bottom left of the TWC envelope, where only a few engine events have been observed (Fig. 11a).

Figures 13(a-d) all display a relatively flat roll-off of TWC_{99} with distance, particularly at scales less than 17.4 Nm. Note that this flattening was not noted in [3] which analyzed the RAE data in a similar manner, but there the minimum distance scale was 4.5 Nm, above which a flattening was not apparent, and below which the distance factor is only an extrapolation. Figure 16 displays the full composite dataset, combined for all temperature intervals (black solid symbols). The Appendix D/P distance factor $df = 1.2595-0.2092log_{10}(dNm)$ is now appropriately applied as a multiplier to the campaign TWC_{99} at 17.4 Nm (dotted magenta line). Although *df* fits the campaign data reasonably well for distance scales greater than approximately 5 Nm, it overestimates TWC_{99} at short distance scales. A new polynomial distance factor, $df2=1.145-0.0574log_{10}(dNm)-0.0366((log_{10}(dNm))^2$, was derived here as a better fit to the campaign data. For the individual temperature ranges (not shown), the new fit is also generally better, particularly for the shorter distance scales. Derivation of individual distance factors for each temperature interval was not considered justifiable given the finite nature of the datasets.

Note that the interpretation of lower distance-scale TWC_{99} values may seem somewhat non-intuitive, as they decreasingly represent upper limits of the dataset as distance scale decreases. This is largely due to the increase in the number of data points. For example, the -50 C composite subset contains 263 and 10312 points at 17.4 Nm and 0.5 Nm respectively. The 99^{th} percentile accordingly drops relative to the maximum value as points increase. The large number of 0.5 Nm points does allow estimation of higher percentiles: for example the 99^{th}, 99.9^{th}, 99.99^{th} percentiles, and maximum at -50 C were 2.10, 2.46, 2.58, and 2.70 gm^{-3}, but adjusting percentile levels with distance scale is an inconvenient way in which to characterize dataset upper limits. For characterization of short-scale high TWC values, the use of the maximum values of Figures 12 (a-d) may therefore be more meaningful depending on the application.

6.5. Particle Distributions and Median Mass Diameters (MMDs).

The campaign results include the first extensive measurements of deep convective cloud high-TWC PSDs and MMDs from modern instrumentation typically used and accepted in the atmospheric science community. The data processing was performed by the Centre National de la Recherche Scientifique (CNRS) and ECCC, and results were synthesized by CNRS. Details on the CNRS data processing method and more detailed results from data subsets have been provided in [45, 59, 7]. In short, PSDs were derived from 2D-S and PIP OAPs described earlier, occasionally substituting alternative instruments if 2D-S and/or PIP measurements were unavailable. The rare mixed-phase periods described in section 6.2 were excluded so as to provide results for ice particles only. The process involved derivation of particle sizes from

individual two-dimensional particle images. Results were accumulated into 5-second spectra of number concentration versus area equivalent diameter (D_{eq}) from 10-12800 μm. Conversion of these into mass spectra required assumptions about the density spectrum of ice particles. Within the atmospheric science community, mass-diameter relationships of the form $m(D)=\alpha D^{\beta}$, have been developed and employed over the years, where α and β are often set as constants and thus the mass spectrum cannot practically adjust to local changes in particle morphology and density that might be expected over a flight. For this study, the CNRS algorithm continually adjusted the β coefficient based on the shape of the two-dimensional images [42], providing an indirect particle density variation. The α coefficient was adjusted so as to provide the same integrated mass as the IKP2. The processing algorithms are complex, incorporating estimation of sizes from irregular particle images, artifact detection and removal, size correction of out-of-focus images, corrections for probe dead time, and other wide ranging technical adjustments. Algorithms used throughout the community use similar techniques. A comparison between CNRS and ECCC algorithms for one Darwin-14 flight, in both stratiform and convective cloud regions, revealed an average MMD difference of less than 4.7% [7], which was considered acceptable for the purposes of this study.

Particles images for the three campaigns were generally irregular in shape, likely composed of individual vapor-grown particles and aggregates, with varying degrees of riming. Heavily rimed particles such as graupel were only occasionally observed, and hail was not encountered.

Rather than providing a 9th percentile MMD, it was decided that a more meaningful statistic would be MMD derived only from high TWC regions of cloud, defined by levels of 1.0 gm^{-3} or higher over distance scales of at least 0.5 Nm. Figure 17 shows average PSDs for such regions, separately for the Falcon-20 (Darwin-14 and Cayenne-2015 combined), the Cayenne-2015 Convair-580, and the Florida-2015 DC-8 for the four temperature intervals. Note that there was general agreement between the data provided by each aircraft within a given temperature interval. As already discussed in [45,7], as temperature increased from -50 to -10 C, the smaller particle concentrations decreased while the larger particle concentrations increased, with the crossover occurring at roughly 500 microns. These studies concluded that the results are consistent with the higher sedimentation rate of the larger ice crystals, and with aggregation becoming more active at warmer temperatures. Figure 18 shows the corresponding data represented as cumulative mass distributions (CMDs). As with the PSDs, there was generally a good agreement between the different aircraft within a given temperature interval, particularly for -50 and -40 C. As per the changes observed in the PSDs, there was less mass concentrated at small sizes, and more at large sizes as temperature increased. Table 5 summarizes the MMDs for the distributions of Figure 18. Falcon-20 and DC-8 MMDs were very similar, and within ±4 % for the -50, -40, and -30 C intervals. The DC-8 lacked sufficient data for comparison at -10 C. The Convair 580 MMD at -10 C was about 15% lower than that of the Falcon-20, an observation that is discussed in section 7. A composite average MMD, weighted to the number of points, is given in the last column, where values increased with increasing temperature from about 326 μm in the -50 C interval to about 708 μm in the -10 C interval. Although higher than the 50-200 μm MMD range specified in Appendix D/P, flight campaign MMDs were still relatively low in these high-TWC regions, particularly in the -30 to -50 C range, as had been speculated at the outset of the flight campaigns. As discussed by [68], secondary ice multiplication processes may have a large impact on maintaining lower MMD values in high IWC cloud regions.

Although the algorithms use the most advanced instruments and techniques commonly used in the atmospheric science community, the methods are complex, and there are unfortunately no comparative reference standards to provide absolute accuracy estimates of the particle CMDs and MMDs of this study. Some recent information on uncertainty has been provided by [69], where Darwin-14 and Cayenne-15 Falcon-20 MMDs computed using a fundamentally different mass retrieval technique were about 10- 20% lower than those listed in this report, depending on temperature.

7. Notes About Global Representativeness of Dataset

The data from the three locations sometimes provided significantly different results, which were apparent from simple visual inspection (e.g. see Figs. 13(a-d)). This may simply be due to the particular combinations of clouds that were available for sampling at each location during each specific period. For example, the Gulf of Mexico clouds sampled in Florida-2015 contained more lightning and high reflectivity at altitude, sometimes requiring sampling further away from active cells in possibly lower TWC. One particularly interesting comparison is for the Convair 580 and Falcon-20 at -10 C in Cayenne-15. These aircraft typically sampled the same general area of clouds at -10 C, sometimes only 30 minutes apart, and presumably should have provided close statistics. The Convair 580 17.4 Nm TWC_{99} values were 24% lower than Falcon-20 values (Fig. 13d), and MMDs were about 15% lower (Table 5). It was concluded that instrument or data processing differences were unlikely to be the cause. One possible explanation is a systematic difference in the choice of track by each aircraft, possibly due to different clearances from active cells preferred by the pilot, or even different pilot radar response providing different indications to the pilot.

Active cells containing significant lightning may have been more frequently avoided than by commercial aviation. Ground lightning network data not normally available to commercial aviation was monitored in real time for this purpose. The intention was to avoid damage to cloud instruments and aircraft, and to enhance flight safety. This may have led to some underestimation of TWC_{99} and mixed phase levels, although it should be noted that in many clouds lightning avoidance was minimal or not required.

All of the measurements were taken during daylight hours, during Darwin-14 and Cayenne-15 to ensure safe aircraft operation, and during Florida-15 because ample targets for the primary HIWC RADAR I objectives were available during the day. There are numerous studies indicating that convective activity over open oceanic regions maximizes overnight due to radiative cooling and destabilization of the cloud top [70-72]. The effect was most noticeable in Darwin-14, where clouds often appeared larger and more active during nighttime hours, consistent with satellite-based climatology of the convective cloud diurnal cycle around Darwin (e.g. [74-76]). In spite of scheduling flight sampling as early as possible after daybreak, a post-campaign study of Darwin-14 satellite IR imagery concluded that sampling was conducted on the average 2.6 hours after the estimated optimum time [9]. The study also concluded that the distance over which high TWC was encountered was likely shorter than what could have been measured earlier, but whether peak TWC would have been higher earlier was unclear. For Cayenne, although an analysis of 20 years of satellite IR images revealed a maximum in deep cloud between 00 and 06 solar time, a manual inspection of IR imagery during the campaign period did not reveal a general presence of larger and/or more active oceanic MCSs before dawn. The measurements were typically taken in the best available oceanic targets of the day or night,

and were sampled within one hour of the estimated optimum time. No similar manual inspection was performed for Florida-15 flights.

The three campaign locations are generally subject to clean atmospheric conditions with low aerosol, due to their distance from significant anthropogenic pollution sources. Convective clouds growing in a high aerosol environment have been shown to nucleate more and smaller cloud droplets [77], and may also develop first ice crystals at a higher altitude [78]). These behaviors may have significant effects on cloud microphysical evolution, including slower conversion of droplets to rain drops and enhanced cloud vertical growth [77], and a higher likelihood of mixed-phase in updrafts [77, 64], at least until widespread precipitation has formed [68]. The effect on TWC is more speculative, although suppression of the early development of rain that is commonly observed in low-aerosol tropical oceanic clouds alone suggests a potential for higher TWC aloft. Curiously, the oceanic regions of southeast Asia and Japan, influenced by industrial regions of China that are likely the world's highest anthropogenic emitters [79], experiences about 39% of Boeing engine events [58]. However the high air traffic density and frequency of deep convective clouds in this region are also likely factors in this high percentage.

The flight campaign dataset is highly dominated by oceanic clouds, with only about 7% from relatively small continental clouds. The earth's most vigorous convective storms occur over land, most notably over the USA, equatorial Africa, and southeast South America [80]. Relative to oceanic storms, they tend to have greater frequency of lightning and high reflectivity at cruise altitudes [80-83]. Up to 41% of engine events occur in such large continental clouds [58]. The South American case studies of [58] showed a median characteristic size of about 200 Nm, defined by IR pixels colder than -50 C, much larger than the continental clouds sampled in the current study. Furthermore, event aircraft more frequently avoided direct penetration of active cells than in the oceanic case studies of [56], perhaps due to greater lightning, high reflectivity or turbulence. Whether aircraft would encounter persistently higher TWCs in such continental MCS, while possibly flying further from active cells than in their oceanic counterparts, is an open question.

The flight campaign datasets represent a snapshot in time from each of the three distantly separated locations. Each was collected in or near the month of maximum convective activity, during years with near normal or somewhat sub-normal surface precipitation [9]. It is unknown whether different TWC statistics would have been collected in a year with abnormally high surface precipitation, although this seems intuitively plausible. Likewise, other geographic locations may have yielded higher TWC statistics. The developers of Appendix C acknowledged the finite nature of their dataset, noting that results were "directly applicable only to the United States" , but the report methods "should provide a framework for placing the data on a statistical basis that is not limited in scope to the United States" [84]. Ultimately Appendix C has been used globally for conventional icing with success and without change, and has withstood the test of time. A similar caution to the current dataset is appropriate. The results should be revisited if and when future datasets become available, particularly those filling data gaps noted above. Global datasets from commercial aircraft, such as those provided by IAGOS (In-Service Aircraft for a Global Observing System; http//www.iagos.org), may ultimately provide such datasets, if the significant instrument and mounting location challenges can be addressed so as to provide high-TWC measurements with an accuracy acceptable to regulators and industry.

8. Summary and Conclusions

A review of results from three international flight campaigns that collected datasets for comparison to the Appendix D/P mixed-phase/glaciated cloud environmental envelope has been provided, condensing material from a variety of project reports. The efforts produced a unique dataset of the in-situ microphysical properties of large deep convective clouds. The campaigns focused on measuring clouds similar to those that have caused ICI engine power loss and damage events. The objectives and methodologies were discussed and approved during meetings between 2004 and 2013 between industry, government research, and regulatory agencies. The data were collected during 54 flights out of one subtropical and two tropical locations, with 472 runs in approximately 115 clouds from about 17,000' to 39,000'. The measurements provide about 29,600 Nm of in situ data in deep convection over four targeted temperature intervals: -10, -30, -40, and -50, all ± 5 C.

The primary cloud target was a Mesoscale Convective System of oceanic origin, with a characteristic size of 100 Nm or greater. Measurements were taken primarily in the warm region of the Appendix D/P temperature-altitude envelope, where most engine events have occurred. The clouds were highly dominated by ice crystals, with only occasional regions of supercooled LWC. Mixed phase comprised less than 5% and 0.2% of the total in-cloud distance at -10 and -30 C, over distance scales less than about 8 Nm, and with average LWC less than 0.32 gm^{-3}. There were no mixed-phase zones colder than -35 C. The campaign results, along with other information from the atmospheric science literature, indicate significantly less frequent mixed-phase, with lower LWC levels, than the upper limits of Appendix D/P "Supercooled Liquid Portion of TWC" specifications, most notably the Appendices' "0.5 gm^{-3} over indefinite length scales." The results however may be specific to the campaigns' very deep oceanic clouds sampled at their mature stage.

Cloud in-situ TWC was measured with a new instrument specifically designed for the high TWC environment. Maximum TWC at the shortest reported 0.5 Nm distance scale reached about 4.1 gm^{-3}. The primary TWC metric for comparison to Appendix D/P was the 99th percentile TWC (TWC_{99}) at the 17.4 Nm distance scale. The three-campaign composite TWC_{99} averaged over 17.4 Nm increased from 1.81 gm^{-3} at -50 C to 2.69 gm^{-3} at -10 C, at a rate similar to, but with values about one half of Appendix D/P. The correlation with the TWC envelope supported a possible simple scale factor adjustment if deemed appropriate, at least for this warm portion of the TWC envelope. The Appendix D/P distance factor overestimated TWC_{99} values at distance scales smaller than about 5 Nm, and a new distance factor was provided for consideration. While Appendix D/P specifies the MMD range of 50-200 µm for particle size, flight campaign values in high TWC conditions, measured with probes with the most recent modifications for mitigation of ice particle shattering artifacts, were larger, increasing with temperature, from about 326 µm at -50 C to about 708 µm at -10 C.

The campaign science team discussed the global representativeness of the dataset to aviation, and noted the following limitations. Lightning was probably avoided more efficiently than by commercial aviation, perhaps lowering TWC_{99} values and levels of mixed-phase. The dataset was collected in daytime hours only. There is a significant body of evidence showing that large tropical convective clouds over the open oceans are most active before dawn. This effect was concluded to be most important for the Darwin data, where the most likely effect was a reduction of length scales over which high TWC was encountered. It was concluded that the effect was minimal for the Cayenne dataset. The data were all collected in regions with relatively clean atmospheres. Clouds in highly polluted atmospheres have been shown to develop with

initially different microphysical properties, and may experience more vertical growth. The effect on flight-level TWC is currently speculative. The dataset also lacks measurements in large continental MCS, which tend to be more vigorous than oceanic, and which currently constitute up to 41% of engine events. Finally, the data were collected at each location during or near peak months of convective activity, and with normal to somewhat sub-normal climatological surface precipitation amounts for the period. Whether periods of abnormally high convective rainfall would have produced more extreme cloud statistics is an open question. The developers of FAR 25 Appendix C cautioned that their results were *applicable only to the regions in which they were collected*, although they are used globally and have stood the test of time. A similar caution is noted here. It would be prudent to revisit the statistics of this study if and when new datasets become available, particularly if they fill gaps in the data identified above.

References

1. "Title 14 Code of Federal Regulations, Part 25 and 33 Appendix D. Airplane and Engine Certification Requirements in Supercooled Large Drop, Mixed Phase, and Ice Crystal Icing Conditions." Docket No. FAA–2010–0636; Amendment Nos. 25–140 and 33–34, published by the Office of the Federal Register, National Archives and Records Administration, Washington, DC. Effective November 4, 2014.
2. "EASA CS 25 Book 1 Appendix P, Annex to Executive Director Decision 2015/008/R of 12 March 2015 Amending Certification Specifications and Acceptable Means of Compliance for Large Aeroplanes CS-25 at Amendment 16,", 2015, https://www.easa.europa.eu/document-library/certification-specifications/cs-25-amendment-16.
3. Mazzawy, Robert S., and Strapp, J. Walter, "Appendix D – An Interim Icing Envelope : High Ice Crystal Concentrations and Glaciated Conditions," *SAE Transactions, Journal of Aerospace*, 116, 634-642, 2007, https://doi.org/10.4271/2007-01-3311.
4. McNaughtan, I. I., "The Analysis of Measurements of Free Ice and Ice/Water Concentrations in the Atmosphere of the Equatorial Zone," Royal Aircraft Establishment (Farnborough) Technical Note No. : Mech. Eng. 283, 1959.
5. FLIGHT INTO ICE CRYSTALS. Aeroplanes and Rotorcraft Joint Airworthiness Committee, Paper 733, Leaflet 714Y, August 1958
6. US Goverrnment Federal Register, 83, No. 12 , Thursday, January 18, 2018.
7. Schwarzenboeck, A., Calmels, A., Coutris, P., Delanoe, J., Dezitter, F., Huet, F., Korolev, A., Leroy, D., McFarquhar, G., Protat, A., and Strapp, J. W., 2018: "Analysis Method Used to Provide All In Situ TWC, IWC, LWC, and Corresponding PSD (As a Function of Maximum and Surface Equivalent Cloud Particle Diameters) Data." EASA Technical Report EASA.2013.FC.27.SC003 EASA HighIWC D3.18 R2.0, 2018.
8. Schwarzenboeck, A., Calmels, A., Coutris, P., Delanoe, J., Dezitter, F., Huet, F., Leroy, D., and Protat, A., "Characterization of In-situ Measured Microphysical Properties in High IWC Regions During the 2014 and 2015 HAIC/HIWC International Field Campaigns." EASA Technical Report EASA.2013.FC.27.SC003 Project, EASA HighIWC D3.19 R2.0, 2018.
9. Strapp, J. W., Schwarzenboeck, A., Bedka, K. , Bond, T. , Calmels, A. , Delanoë, J. , Dezitter, F. , Grzych, M. , Harrah, S. , Korolev, A. , Leroy, D. , Lilie, L. , Mason, J. , Potts, R. , Protat, A. , Ratvasky, T. , Riley, J. , and Wolde, M., "An Assessment of Cloud Total Water Content and Particle Size from Flight Test Campaign Measurements in High Ice Water Content, Mixed Phase/Ice Crystal Icing Conditions: Primary In-Situ Measurements," FAA Rep. DOT/FAA/TC-18/1, in publication process, 2020.
10. "In-flight Icing Encounter and Loss of Control Simmons Airlines, d.b.a. American Eagle Flight 4184 Avions de Transport Regional (ATR) Model 72-212, N401AM, Roselawn, Indiana October 31, 1994; Volume 1," NTSB/AAR-96-01, 1996.
11. "In-flight Icing Encounter and Loss of Control Simmons Airlines, d.b.a. American Eagle Flight 4184 Avions de Transport Regional (ATR) Model 72-212, N401AM, Roselawn, Indiana October 31, 1994; Volume II," NTSB/AAR-96-02, 1996.
12. National Transportation Safety Board Safety Recommendation A-96-54, August 15, 1996.
13. American Meteorological Society, cited 2016, "Supercooled Large Drops", Glossary of Meteorology, available online at https://glossary.ametsoc.org/wiki/Supercooled_large_drops
14. "Title 14 Code of Federal Regulations, Airworthiness Standards: Transport Category Airplanes Appendix O to Part 25 – Supercooled Large Drop Icing Conditions." Docket No. FAA–2010–0636; Amendment No. 25–140, 79 FR 65528, published by the Office of the Federal Register, National Archives and Records Administration, Washington, DC. Effective November 4, 2014.
15. Bowden, D.T., Gensemer, A.E., and Speen, C.A., "Engineering Summary of Airframe Icing Technical Data. FAA Technical Report ADS-4," 1965, http://www.dtic.mil/dtic/tr/fulltext/u2/608865.pdf.
16. Gibb, W.F., "Chasing the Ice Gremlin," FLIGHT, 4 Apr. 1958.
17. Lawson, R.P., Angus, L.J., and Heymsfield, A.J., "Cloud Particle Measurements in Thunderstorm anvils and Possible Threat to Aviation," *J. Aircraft*, 35, No. 1, pp. 113-121, 1998, https://doi.org/10.2514/2.2268.

18. FAA Docket No. 96-NM-162-AD; Amendment 39-9694; AD 96-14-09. Airworthiness Directives: British Aerospace Model BAe 146-100A, -200A, and -300A Series Airplanes, 1996.
19. FAA Docket No. 96-NM-162-AD; Amendment 39-9694; AD 96-14-09. Cancellation. http://rgl.faa.gov/Regulatory_and_Guidance_Library/rgad.nsf/0/0FC9B18C4E49D19886256A0A00736F22?OpenDocument, 1996.
20. FAA Docket No. 98-ANE-42-AD; Amendment 39-11225; AD 99-15-06, 1999, http://rgl.faa.gov/Regulatory_and_Guidance_Library/rgad.nsf/0/61A90814DF6196668625686200744 0B8?OpenDocument&Highlight=96-14-09.
21. FAA Docket No. 98-ANE-42-AD; Amendment 39-11225; AD 99-15-06, 1999, http://rgl.faa.gov/Regulatory_and_Guidance_Library/rgad.nsf/0/61A90814DF6196668625686200744 0B8?OpenDocument&Highlight=94-07-09.
22. FAA Docket No. 98-ANE-42-AD; Amendment 39-11225; AD 99-15-06, 1999, http://rgl.faa.gov/Regulatory_and_Guidance_Library/rgad.nsf/0/61A90814DF6196668625686200744 0B8?OpenDocument&Highlight=99-15-06.
23. Mason, J., Strapp J.W. and Chow P., "The Ice Particle Threat to Engines in Flight," 44th AIAA Aerospace Sciences meeting and Exhibit, Reno, Nevada AIAA 2006-206, 2006, https://doi.org/10.2514/6.2006-206.
24. Strapp, J.W., Chow, P., Maltby, M., Bezer, A.D., Korolev, A., Stromberg, I., and Hallett, J., "Cloud Microphysical Measurements in Thunderstorm Outflow Regions during Allied/BAe 1997 Flight Trials, 37th AIAA Aerospace Sciences Meeting and Exhibit , Reno, NV , AIAA 99-0498., 1999, https://doi.org/10.2514/6.1999-498.
25. Duviver, E., "High Altitude Icing Environment," Intl. Air Safety and Climate Change Conf., 8-9 Sep. 2010, Cologne, DE, available from https:// www.easa.europa.eu/conferences/iascc/doc/.
26. Abraham, J., Strapp, J. W., Fogarty, C., and Wolde, M., " Extratropical Transition of Hurricane Michael," *Bull. Amer. Met. Soc.,* 85, 1323-1339, 2004, https://doi.org/10.1175/BAMS-85-9-1323.
27. Korolev, A.V., Emery, E. F., Strapp, J. W., Cober, S. G., Isaac, G. A., Wasey, M. , and Marcotte, D., "Small Ice Particles in Tropospheric Clouds: Fact or Artifact? Airborne Icing Instrumentation Evaluation Experiment," *Bull. Amer. Met. Soc*., 92, 967-973, 2011, https://doi.org/10.1175/2010BAMS3141.1.
28. Grandin, A., Merle, J-M, Weber, M., Strapp, J.W., Protat, A., and King, P., "AIRBUS Flight Tests in High Total Water Content Regions," 6th AIAA Atmospheric and Space Environments Conference, AIAA AVIATION Forum, AIAA 2014-2753, 2014, http://dx.doi.org/10.2514/6.2014-2753.
29. Dezitter, F., Grandin, A., Brenguier, J.-L., Hervy, F., Schlager, H., Villedieu, P., and Zalamansky, G., "HAIC - High Altitude Ice Crystals," 5th AIAA Atmospheric and Space Environments Conference, American Institute of Aeronautics and Astronautics, 2013, http://arc.aiaa.org/doi/abs/10.2514/6.2013-2674.
30. Strapp, J. W., Isaac, G.A., Korolev, A., Ratvasky, T. P., Potts, R., May, P., Protat, A., Minnis, P., Ackerman, A., Fridlind, A., Haggerty, J., and Riley, J., "The High Ice Water Content (HIWC) Study of Deep Convective Clouds: Science and Technical Plan.," FAA Rep. DOT/FAA/TC-14/31, 105 pps., 2016,http://www.tc.faa.gov/its/worldpac/techrpt/tc14-31.pdf.
31. Ratvasky, T.P., Harrah, S. D., Strapp, J. W., Lilie, L.E., Proctor, F.H., Strickland, J. K., Hunt, P. J., Bedka, K. M., Diskins, G. S., Nowak, J. B., Bui, T. V., Bansemer, A., and Dumont, C. J., "Summary of the High Ice Water Content (HIWC) RADAR Flight Campaigns," SAE Technical Paper 2019-01-2025, NASA/TM-2020-220306, 2019, https://doi.org/10.4271/2019-01-2027.
32. Bravin, M., Strapp, J.W., and Mason, J.G., "An Investigation into Location and Convective Lifecycle Trends in an Ice Crystal Icing Engine Event Database," SAE Technical Paper 2015-01-2130*,* 2015, https://doi.org/10.4271/2015-01-2130.
33. Wolde, M., Nguyen C., Korolev A., and Bastian M., "Characterization of the Pilot X-band Radar Responses to the HIWC Environment during the Cayenne HAIC-HIWC 2015 Campaign," 8th AIAA Atmospheric and Space Environments Conference. AIAA Aviation, AIAA 2016-4201, 2016, https://doi.org/10.2514/6.2016-4201.
34. Baumgardner, D., Brenguier, J.-L., Bucholtz, A., Coe, H., DeMott, P., Garrett, T. J., Gayet, J.-F., Hermann, M., Heymsfield, A., Korolev, A. V., Krämer, M., Petzold, A., Strapp, W., Pilewskie, P., Taylor, J. P., Twohy, C., Wendish, M., Bachalo, W. D., Chuang, P., "Airborne Instruments to Measure Atmospheric Aerosol Particles, Clouds and Radiation: A Cook's Tour of Mature and Emerging Technology," *Atmos. Res.*, 102, 10–29, 2011, https://doi.org/10.1016/j.atmosres.2011.06.021.
35. Davison, C. R., MacLeod, J. D., Strapp, J. W., and Buttsworth, D. R., "Isokinetic Total Water Content Probe in a Naturally Aspirating Configuration: Initial Aerodynamic Design and Testing*"* 46th AIAA Aerospace Sciences Meeting and Exhibit, Reno, NV, AIAA-2008-0435, 2008, doi: 10.2514/6.2008-435.
36. Davison, C. R., MacLeod, J. D., Strapp, J. W., "Naturally Aspirating Isokinetic Total Water Content Probe: Evaporator Design and Testing," 1st AIAA Atmospheric and Space Environments Conference*,* San Antonio, Texas, AIAA-2009-3861, 2009, doi: 10.2514/6.2009-3861.
37. Davison, C. R., Landreville, C., MacLeod, J. D., "Initial Development and Testing of Isokinetic Probe to Measure Total Water Content during Ground and Airborne Testing, NRC Report LTR-GTL-2010-0002, 2010.
38. Davison, C. R., MacLeod, J. D., and Ratvasky, T. P., "Naturally Aspirating Isokinetic Total Water Content Probe: Preliminary Test Results and Design Modifications," 2nd AIAA Atmospheric and Space Environments Conference, Toronto, Ontario. AIAA-2010-7530, 2010, https://doi.org/10.2514/6.2010-7530.

39. Davison, C. R., Ratvasky, T. P., Lilie, L. E., "Naturally Aspirating Isokinetic Total Water Content Probe: Wind Tunnel Test Results and Design Modifications," SAE 2011 International Conference on Aircraft and Engine Icing and Ground Deicing, Chicago, IL, SAE 2011-38-0036, 2011, https://doi.org/10.4271/2011-38-0036.
40. Davison, C. R., Strapp, J. W., Lilie, L. E., Ratvasky, T.P., and Dumont, C., "Isokinetic TWC Evaporator Probe: Calculations and Systemic Uncertainty Analysis," 8th AIAA Atmospheric and Space Environments Conference, Washington, D.C., AIAA-2016-4060, 2016, https://doi.org/10.2514/6.2016-4060.
41. Strapp, J. W., Lilie, L. E., Ratvasky, T. P., Davison, C. R., and C. Dumont, "Isokinetic TWC Evaporator Probe: Development of the IKP2 and Performance Testing for the HAIC-HIWC Darwin 2014 and Cayenne Field Campaigns", 8th AIAA Atmospheric and Space Environments Conference, Washington, D.C., AIAA 2016-4059, 2016, http://dx.doi.org/10.2514/6.2016-4059.
42. Strapp, J. W., MacLeod, J. D., and Lilie, L. E., "Calibration of Ice Water Content in a Wind Tunnel / Engine Test Cell Facility," 15th Inter. Conf. On Clouds and Precipitation, Cancun, Mexico, 2008.
43. Lance, S., Brock, C. A., Rogers, D., and Gordon, J. A., "Water Droplet Calibration of the Cloud Droplet Probe (CDP) and In-Flight Performance in Liquid, Ice and Mixed-Phase Clouds during ARCPAC," *Atmos. Meas. Tech.*, 3, 1683-1706, doi:10.5194/amt-3-1683-2010, 2010.
44. Lawson, R. P., O'Connor, D., Zmarzly, P., Weaver, K., Baker, B. A., Mo, Q., and Jonsson, H., "The 2D-S (Stereo) Probe: Design and Preliminary Tests of a New Airborne, High Speed, High-Resolution Particle Imaging Probe," *J. Atmos. Oceanic Technol.*, 23, 1462-1477, 2006, https://doi.org/10.1175/JTECH1927.1.
45. Leroy, D., Fontaine, E., Schwarzenboeck, A., and Strapp, J. W., "Ice Crystal Sizes in High Ice Water Content Clouds. Part I: On the Computation of Median Mass Diameters from In Situ Measurements," *J. Atmos. Oceanic Technol.*, 33, 2461–2476, 2016, doi: https://doi.org/10.1175/JTECH-D-15-0151.1.
46. Korolev, A., and Isaac, G. A., "Shattering during Sampling by OAPs and HVPS. Part I: Snow Particles." *J. Atmospheric Ocean. Technol.*, 22, 528–542, 2005, doi:10.1175/JTECH1720.1.
47. Field, P. R., Heymsfield, A. J., and Bansemer, A., "Shattering and Particle Interarrival Times Measured by Optical Array Probes in Ice Clouds," *J. Atmospheric Ocean. Technol.*, 23, 1357–1371, 2006, doi:10.1175/JTECH1922.1.
48. Lawson, R.P., "Effects of Ice Particles Shattering on the 2D-S Probe." *Atmos. Meas. Tech.,* 4, 1361-1381, 2011, https://doi.org/10.5194/amt-4-1361-2011.
49. Korolev, A.V., and Field, P. R., "Assessment of the Performance of the Inter-arrival Time Algorithm to Identify Ice Shattering Artifacts in Cloud Particle Probe Measurements," *Atmos. Meas. Tech.*, 8, 761–777, 2015, doi:10.5194/amt-8-761-2015.
50. Korolev, A. V., "Probe Tips for Airborne Instruments Used to Measure Cloud Microphysical Parameters," United States Patent No. 7,861,584, Issued: January 4, 2011, Owner: Her Majesty the Queen in Right of Canada, as Represented by The Minister of Environment, 2011.
51. Korolev, A. V., Emery, E., and Creelman, K., "Modification and Tests of Particle Probe Tips to Mitigate Effects of Ice Shattering," *J. Atmos. Oceanic Technol.*, 30, 690–708, 2013, https://doi.org/10.1175/JTECH-D-12-00142.1.
52. Korolev, A. V., McFarquhar, G., Field, P. R., Franklin, C., Lawson, P., Wang, Z., Williams ,E., Abel, S. J., Axisa, D., Borrmann, S., Crosier, J., Fugal, J., Krämer, M., Lohmann, U., Schlenczek, O., Schnaiter, M., and Wendisch, M., " Mixed-Phase Clouds: Progress and Challenges," *Meteorol. Monogr.,*58, 5.1-5.50. 2017, doi:10.1175/AMSMONOGRAPHS-D-17-0001.1.
53. Baumgardner, D., and Rodi, A., "Laboratory and Wind Tunnel Evaluations of the Rosemount Icing Detector," *J. Atmos. Oceanic Technol.,*6, 971–979, 1989, https://doi.org/10.1175/1520-0426(1989)006<0971:LAWTEO>2.0.CO;2.
54. Korolev, A. V., Strapp, J. W., and Isaac, G. A., "The Nevzorov Airborne Hot-Wire LWC-TWC Probe: Principle of Operation and Performance Characteristics," *J. Atmos. Ocean. Technol.*, 15, 1495–1510, 1998, https://doi.org/10.1175/1520-0426(1998)015<1495:TNAHWL>2.0.CO;2.
55. Gryzch, M. and Mason, J. G., "Weather Conditions Associated with Jet Engine Power Loss and Damage Due to Ingestion of Ice Particles: What We've Learned Through 2009," 14th Conference on Aviation, Range and Aerospace Meteorology, AMS, Atlanta, GA, 2010.
56. Mason, J.G., and Grzych, M., "The Challenges Identifying Weather Associated with Jet Engine Ice Crystal Icing," *SAE Transactions, Journal of Aerospace*, SAE Technical Paper 2011-38-0094, 2011. doi:10.4271/2011-38-0094.
57. Grzych, M., Tritz, T., Mason, J. G., Bravin, M., and Sharpsten, A., "Studies of Cloud Characteristics Related to Jet Engine Ice Crystal Icing Utilizing Infrared Satellite Imagery," SAE Technical Paper 2015-01-2086, 2015, doi:10.4271/2015-01-2086.
58. Bravin, M. and Strapp, J.W., "A Continuing Investigation of Diurnal and Location Trends in an Ice Crystal Icing Engine Event Database," SAE Int. J. Advances & Curr. Prac. in Mobility 2(1):90-105, 2020, doi:10.4271/2019-01-1964.
59. Leroy, D., Coutris, P., Fontaine, E., Schwarzenboeck, A., Strapp, J. W, Lilie, L. E., Korolev, A. V., McFarqhuar, G., and Dezitter, F., "HAIC/HIWC Field Campaigns - Specific Findings on Ice Crystals Characteristics in High Ice Water Content Cloud Regions," 8th AIAA Atmospheric and Space Environments Conference, AIAA Aviation, AIAA 2016-4056, 2016, http://dx.doi.org/10.2514/6.2016-4056.
60. Cober, S. G., Isaac, G. A., Korolev, A. V., and Strapp, J. W., "Assessing Cloud-Phase Conditions," *J. Appl. Meteor.*, 40, 1967–1983, 2001, doi:10.1175/1520-0450(2001)040<1967:ACPC>2.0.CO;2.

61. Stith, J. L., Dye, J. E., Bansemer, A., Heymsfield, A., Grainger, C., Petersen, W. W., and Berticelli, R., "Microphysical Observations of Tropical Clouds," *J. Appl. Meteor.*,41, 97-117, 2002, https://doi.org/10.1175/1520-0450(2002)041<0097:MOOTC>2.0.CO;2.
62. Black, R. and Hallett, J., "Observations of the Ice Distributions in Hurricanes," *J. Atmos. Sci.,* 43, 802-822, 1986, https://doi.org/10.1175/1520-0469(1986)043<0802:OOTDOI>2.0.CO;2.
63. McFarquhar, G. M., and Heymsfield, A. J., "Microphysical Characteristics of Three Anvils Sampled during the Central Equatorial Pacific Experiment, *J. Atmos. Sci.*, 53, 2401–2423, 1996, doi:10.1175/1520-0469.053<2401:MCOTAS>2.0.CO;2.
64. Lawson, P., Gurganus, C., Woods, S., and Bruintjes, R., "Aircraft Observations of Cumulus Microphysics Ranging from the Tropics to Midlatitudes: Implications for a 'New' Secondary Ice Process," *J. Atmos. Sci.*, 74, 2899–2920, 2017, https://doi.org/10.1175/JAS-D-17-0033.1.
65. Rosenfeld, D., Woodley, W. L., Krauss, T. W., and Makitov, V., "Aircraft Microphysical Documentation from Cloud Base to Anvils of Hailstorm Feeder Clouds in Argentina," *J. Appl. Meteor. Climatol.*, 45, 1261–1281, 2006, https://doi.org/10.1175/JAM2403.1.
66. NIST/SEMATECH e-Handbook of Statistical Methods. http://www.itl.nist.gov.div898/handbook/, section 7.2.6.2, April 2012.
67. Bouchard, A., Lalande, P., Laroche, P., Blanchet, P., Buguet, M., Chazottes, A., and Strapp, J. W., "Relationship Between Airborne Electrical and Total Water Content Measurements in Ice Clouds," *Atmospheric Research*, 237:104836, 2019, doi: 10.1016/j.atmosres.2019.104836.
68. Korolev, A. V., Heckman, I., Wolde, M., Ackerman, A. S., Fridlind, A. M., Ladino, L. A., Lawson, R. P., Milbrandt, J., and Williams, E., "A New Look at the Environmental Conditions Favorable to Secondary Ice Production," *Atmos. Chem. Phys.*, 20, 1391–1429, 2020, https://doi.org/10.5194/acp-20-1391-2020.
69. Coutris, P., Schwarzenboeck, A., Leroy, D., Grandin, A., Dezitter, F., and Strapp, J. W., 2019, "Uncertainty of the Ice Particles Median Mass Diameters Retrieved from the HAIC-HIWC Dataset: A Study of the Influence of the Mass Retrieval Method," SAE Int. J. Adv. & Curr. Prac. in Mobility 2(1):140-150, 2020, https://doi.org/10.4271/2019-01-1983.
70. Allbright, M. D., Recker, E. R., Reed, R. J., and Dang, R., "The Diurnal Variation of Deep Convection and Inferred Precipitation in the Central Tropical Pacific during January-February 1979." *Mon. Wea. Rev.*, 113 1663-1680, 1985, https://doi.org/10.1175/1520-0493(1985)113<1663:TDVODC>2.0.CO;2.
71. Randall, D.A., Harshvardhan, and Dazlich, D.A., "Diurnal Variability of the Hydrological Cycle in a GCM," *J. Atmos.Sci.*, 48, 40-62, 1991, https://doi.org/10.1175/1520-0469(1991)048<0040:DVOTHC>2.0.CO;2.
72. Chen, S. S., and Houze, R. A. Jr., "Diurnal Variation and Life Cycle of Deep Convective Systems over the Tropical Pacific Warm Pool," *Quart. J. Roy. Meteor. Soc.*, 123, 357-388, 1997, https://doi.org/10.1002/qj.49712353806.
73. Liu, C., Zipser, E.J., "Diurnal Cycles of Precipitation, Clouds, and Lightning in the Tropics from 9 years of TRMM Observations," *Geophys. Res. Letters*, 35, L04819, 2008, doi:10.1029/2007GL032437.
74. Murakami, M., "Analysis if the Deep Convective Activity Over the Western Pacific and Southeast Asia, Part 1: Diurnal Variation," *J. Met. Soc. Japan*, 61, 60-76, 1983, https://doi.org/10.2151/jmsj1965.61.1_60
75. May, P. T., Long, C., and Protat, A., "The Diurnal Cycle of the Boundary Layer, Convection, Clouds, and Surface Radiation in a Coastal Monsoon Environment (Darwin, Australia)," *J. Climate*, 25, 5309-5326, 2012, https://doi.org/10.1175/JCLI-D-11-00538.1.
76. Protat, A., Rauniyar, S., Kumar, V. V., and Strapp, J. W., "Optimizing the Probability of Flying in High Ice Water Content Conditions in the Tropics Using a Regional-Scale Climatology of Convective Cell Properties," *J. Appl. Meteor. Clim.*, 53 (11), 2438-2456, 2014, https://doi.org/10.1175/JAMC-D-14-0002.1.
77. Rosenfeld, D., Lohmann, U., Raga, G. , O'Dowd, C., Kulmala, M., Fuzzi, S., Reissell, A., and Andreae, M., "Flood or Drought: How do Aerosols Affect Precipitation?," *Science*, v.321, 1309-1313, 321, 2008, doi: 10.1126/science.1160606.
78. Braga, R. C., Rosenfeld, D., Weigel, R., Jurkat, T., Andreae, M. O., Wendisch, M., Pöschl, U., Voigt, C., Mahnke, C., Borrmann, S., Albrecht, R. I., Molleker, S., Vila, D. A., Machado, L. A. T., and Grulich, L., "Further Evidence for CCN Aerosol Concentrations Determining the Height of Warm Rain and Ice Initiation in Convective Clouds over the Amazon Basin," *Atmos. Chem. Phys.*, 17, 14433–14456, 2017, https://doi.org/10.5194/acp-17-14433-2017.
79. Forster, P., Ramaswamy, V., Artaxo, P., Berntsen, T., Betts, R., Fahey, D.W., Haywood, J., Lean, J., Lowe, D. C., Myhre, G., Nganga, J., Prinn, R., Raga, G., Schulz, M., and Dorland, R.V., "Changes in Atmospheric Constituents and in Radiative Forcing, in Climate Change 2007: The Physical Science Basis. Contribution of Working Group I to the Fourth Assessment Report of the Intergovernmental Panel on Climate Change, edited by S. Solomon, D. Qin, M. Manning, Z. Chen, M. Marquis, K.B. Averyt, M.Tignor, and H.L. Miller, Cambridge University Press, United Kingdom and New York, NY, USA, 2007.
80. Zipser, E.J., Liu, C., Cecil, D.J., Nesbitt, S.W., and Yorty, D.P., "Where Are the Most Intense Thunderstorms on Earth?," *Bull. Amer. Meteor. Soc.*, 87, 1057–1071, 2006, doi: 10.1175/BAMS-87-8-1057.
81. Zipser, E.J., and Lutz, K.R., "The Vertical Profile of Radar Reflectivity of Convective Cells: A Strong Indicator of Storm Intensity and Lightning Probability?," *Mon. Wea. Rev.*, 122, 1751–1759, 1994, https://doi.org/10.1175/1520-0493(1994)122<1751:TVPORR>2.0.CO;2.
82. Orville, R.E., and Henderson, R.W., "Global Distribution of Midnight Lightning: September 1977 to August 1978," *Mon. Wea. Rev.*, 114, 2640–2653, 1986, https://doi.org/10.1175/1520-0493(1986)114<2640:GDOMLS>2.0.CO;2.

83. Zipser, E.J. "Deep Cumulonimbus Cloud Systems in the Tropics with and without Lightning," *Mon. Wea. Rev.*, 122, 1837–1851, 1994, https://doi.org/10.1175/1520-0493(1994)122<1837:DCCSIT>2.0.CO;2.
84. Lewis, W. and Bergrun, N. R., "A Probability Analysis of the Meteorological Factors Conducive to Aircraft Icing in the United States," NACA Tech. Note 2738, 93 pp., 1952, https://digital.library.unt.edu/ark:/67531/metadc53548/: accessed June 15, 2020, University of North Texas Libraries, UNT Digital Library, https://digital.library.unt.edu; crediting UNT Libraries Government Documents Department.

Acknowledgments

Major North American funding for flight campaigns and associated research was provided by the FAA William Hughes Technical Center and Aviation Weather Research Program, the NASA Aeronautics Research Mission Directorate Aviation Safety Program, the Boeing Co., Environment and Climate Change Canada, the National Research Centre (NRC)of Canada, and Transport Canada . Major European campaign and research funding was provided by (i) the European Commission Seventh Framework Program in research, technological development and demonstration under grant agreement n°ACP2-GA-2012-314314, and (ii) the European Aviation Safety Agency (EASA) Research Program under service contract n° EASA.2013.FC27. Further funding was provided by the Ice Crystal Consortium.

The authors wish to thank the following for additional project management support: Chris Dumont, FAA; Ron Colantonio, NASA Aerosciences Evaluation & Test Capabilities Project Manager; Peter May, Australian Bureau of Meteorology.

Operational support for the research aircraft is acknowledged as follows. For the Falcon-20, primary support was provided by the SAFIRE facility for scientific airborne operations. SAFIRE (http://www.safire.fr) is a joint facility of CNRS, Météo-France and CNES. For the Convair 580, primary support was provided by the Flight Research Laboratory of the NRC Aerospace Research Centre, and the Environment and Climate Change Canada Observation Based Research Section. For the NASA DC-8, primary support was provided by the NASA Armstrong Flight Research Center.

Other operational support during flight campaigns was provided by: the Australian Bureau of Meteorology (local facilities in Darwin, campaign-dedicated and operational Northern Territories Weather Office forecasters); Meteo France, the NASA Langley Cloud and Radiation Research Group (nowcasting and real-time and archive of satellite products); the National Center for Atmospheric Research (nowcasting and data archiving); the NASA Langley Electromagnetic Sensors Branch (pilot radar research); and the Boeing Company, ATMOSPHERE, Coriolis Weather, and Leading Edge Atmospherics (dedicated real-time forecasting).

The Japan Meteorological Agency is specially thanked for providing rapid-scan visible and infrared MTSAT-1R satellite data during the Darwin-2014 campaign.

Definitions/Abbreviations

2D-S	Two-dimensional Stereo Optical Array Spectrometer (Stratton Park Engineering Co.)
ARAC	Aviation Rulemaking Advisory Committee
BWV	Background Water Vapor
Cayenne-15	HAIC-HIWC Cayenne-2015 flight campaign

CDP-2	Cloud Droplet Probe (Droplet Measurement Technologies) – version 2
CMD	Cumulative Mass Distribution (ice particle)
CNRS	Centre National de la Recherche Scientifique
Darwin-14	HAIC-HIWC Darwin-2014 flight campaign
d50	Cloud approximate area equivalent diameter for IR temperatures colder than -50 C (see Table 1 caption for definition)
D	Diameter, general (particle)
D_{eq}	Area equivalent diameter (particle)
Df	Distance Factor for Appendix D/P TWC_{99}
DMT	Droplet Measurement Technologies
EASA	European Aviation Safety Agency
EHWG	Engine Harmonization Working Group
EIWG	Engine Icing Working Group
ECCC	Environment and Climate Change Canada
FAA	Federal Aviation Administration
Florida-15	HIWC RADAR I 2015 flight campaign
FSSP-100	Forward Scattering Spectrometer Probe (model 100)
HAIC	High Altitude Ice Crystals (project)
HIWC	High Ice Water Content (project)
IAGOS	In-Service Aircraft for a Global Observing System
ICI	Ice Crystal Icing
IKP-2	Isokinetic Evaporator Probe (flight campaigns)
ITCZ	Intertropical Convergence Zone
IR	Infrared
IWC	Ice Water Content (mass concentration of ice particles)
JAC	Joint Airworthiness Committee
JMA	Japan Meteorological Agency

LWC	Liquid Water Content
m(D)	Mass of particle of diameter D
MCS	Mesoscale Convective System
MMD	Median Mass Diameter
MTSAT	Multifunctional Transport Satellites (Japan)
NASA	National Aeronautics and Space Administration
Nm	Nautical mile
NRC	National Research Council (Canada)
NTSB	National Transportation Safety Board
PIP	Precipitation Imaging Probe (Droplet Measurement Technologies)
PSD	Particle Size Distribution
RAE	Royal Aircraft Establishment
SAFIRE	Service des Avions Français Instrumentés pour la Recherche en Environnement
SEA	Science Engineering Associates
SPEC	Stratton Park Engineering Co.
SLD	Supercooled Large Drops
TAT	Total Air Temperature
TWC	Total Water Content
TWC_{99}	99th percentile TWC

TABLES

	Darwin-14	Cayenne-15	Florida-15	Boeing engine events[!+]	Boeing engine events south-east Asia[#]
MCS cloud size d50 (for IR ≤-50 C) Median, Nm	210	100	160	n/a	n/a
MCS distance across "enhanced region" (for IR area ≤ equilibrium temperature) Median, Nm	105[+]	n/a	n/a	130[+]	137
Cloud Top minimum IR Temperature Median, C	-80	-62	-61	-63[!]	-84
Atmospheric Precipitable Water Day median, mm	60	58	51	58[!]	64

Table 1. General cloud and atmospheric properties during the project sampling, and comparison to engine events, adapted from [9]. The cloud size d50 is approximated from the cloud satellite IR elliptical area ≤ -50 C, where d50= $(d_{ns} \cdot d_{ew})^{0.5}$, and d_{ns} and d_{ew} are the north-south and east west distances visually estimated across this area at the midpoint of the sampling time. Boeing engine event statistics for "enhanced regions"(see text) as follows: [!] 46 events from [52]; [#] 11 southeast Asia events from [32]; [+] 52 MCS events from [57].

	Darwin-14 Falcon-20	**Cayenne-15 Falcon-20**	**Cayenne-15 Convair-580**	**Florida-15 NASA DC-8**	**All Projects**
-10 C (-15 < T ≤ -5)	12	101	153	5	271
-20 C (-25 < T ≤ -15)	17	26	1	0	44
-30 C (-35 < T ≤ -25)	141	130	0	174	445
- 40 C (-45 < T ≤ -35)	187	111	0	136	434
-50 C (-55 < T ≤ -45)	30	55	0	178	263
All temperature intervals	387	423	158	493	1461

Table 2. Number of 17.4 Nm data points collected within each temperature interval, by project, from [9]. The "all temperature intervals" row includes a few additional points for > -5 C for the Convair-580.

			M-P length scale		M-P LWC	
Campaign Dataset	SAT ±5 C	% dist. in M-P	Median Nm	Max. Nm	Median gm^{-3}	Max. gm^{-3}
Convair 580 Cayenne-2015	-10	≤ 5%	-	-	-	≤ 0.25
Falcon-20 Darwin-14 plus Cayenne-15	-10	2.8%	1.8	7.9	0.08	0.32
	-30	0.2%	0.9	3.4	0.10	0.12
	-40	0	0	0	0	0
DC-8 Florida-2015	ALL	N/A	N/A	N/A	N/A	N/A

Table 3. Mixed-phase (M-P) results from the three campaigns. Temperature intervals are defined in Table 2.

Temperature Range- deg C	Horizontal cloud length – nautical miles	LWC – g/m^3
0 to -20 ……..	≤50 ……..	≤1.0
0 to -20 ……..	Indefinite ……..	≤0.5
< -20 ……..	……..	0

Table 4. Supercooled Liquid Portion of TWC for Appendix D/P [1,2], originally from [3]

	Falcon-20 (Darwin-14 and Cayenne-15)	DC-8 (Florida-15)	Convair 580 (Cayenne-15)	Composite avg.
-50 C MMD (μm)	316	329	No data	**326**
-40 C MMD (μm)	401	381	No data	**396**
-30 C MMD (μm)	476	493	No data	**483**
-10 C MMD (μm)	747	Minimal data	630	**708**

Table 5. Median Mass Diameters (MMDs) of the ice particle cumulative mass distributions of Figure 18. A composite arithmetic number-weighted average MMD is given in the last column. Adapted from [8] with Convair 580, with composite data added. Temperature intervals are defined in Table 2.

FIGURES

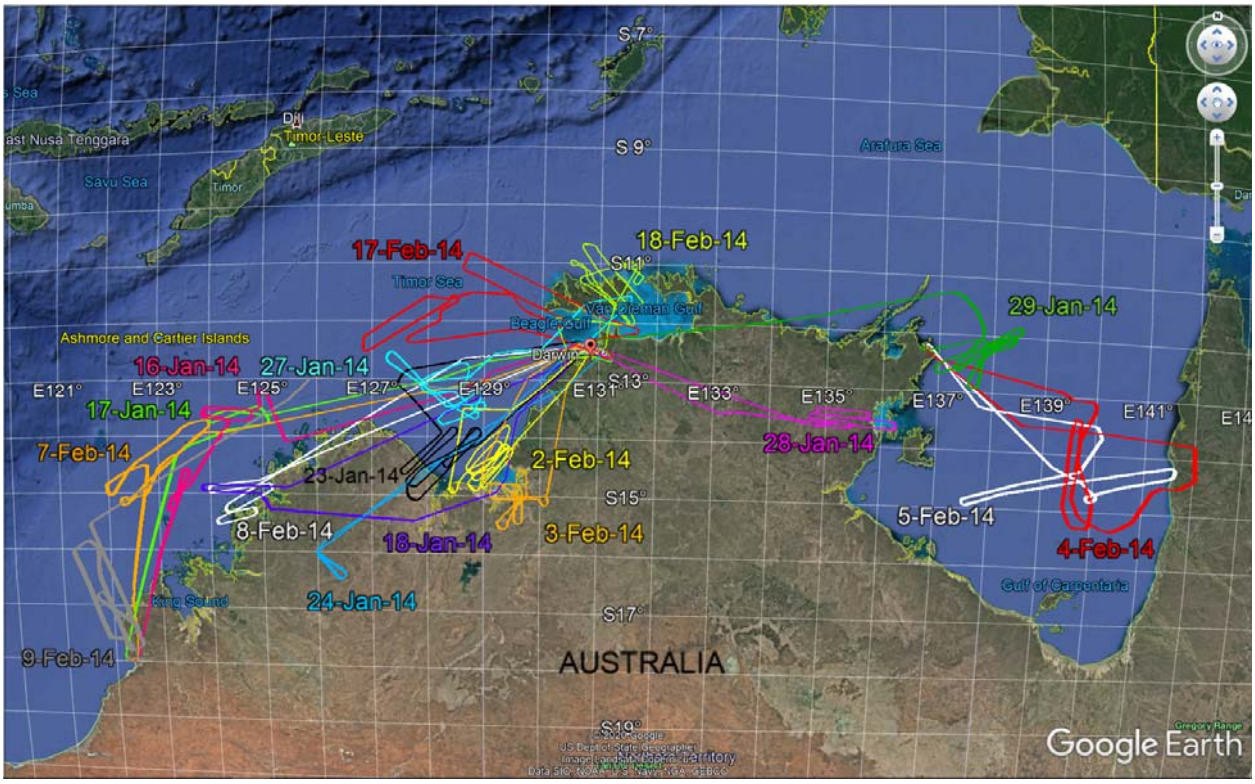

Figure 1. Seventeen flight tracks of the Falcon-20 research aircraft contributing data to the Appendix D/P assessment, during the HAIC-HIWC "Darwin-14" flight campaign out of Darwin, Australia. Adapted from [9]. Flights were conducted during the period of 16 Jan. – 18 Feb., 2014. Individual flights are delineated by separate colors, with UTC date identifiers of the same colour.

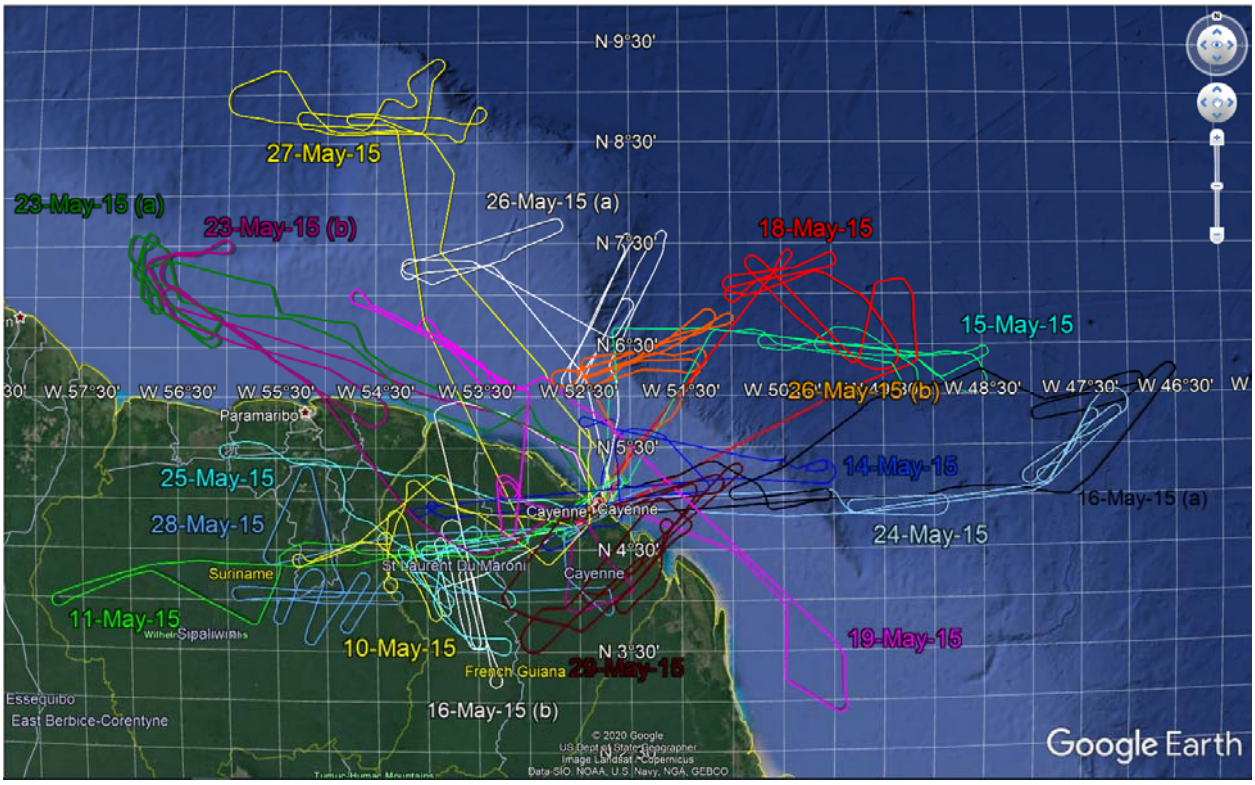

Figure 2. As in Fig. 1, but for seventeen SAFIRE Falcon-20 flights contributing to the Appendix D/P comparison during the HAIC-HIWC "Cayenne-15" flight campaign out of Cayenne, French Guiana from 5-29 May, 2015. Adapted from [9].

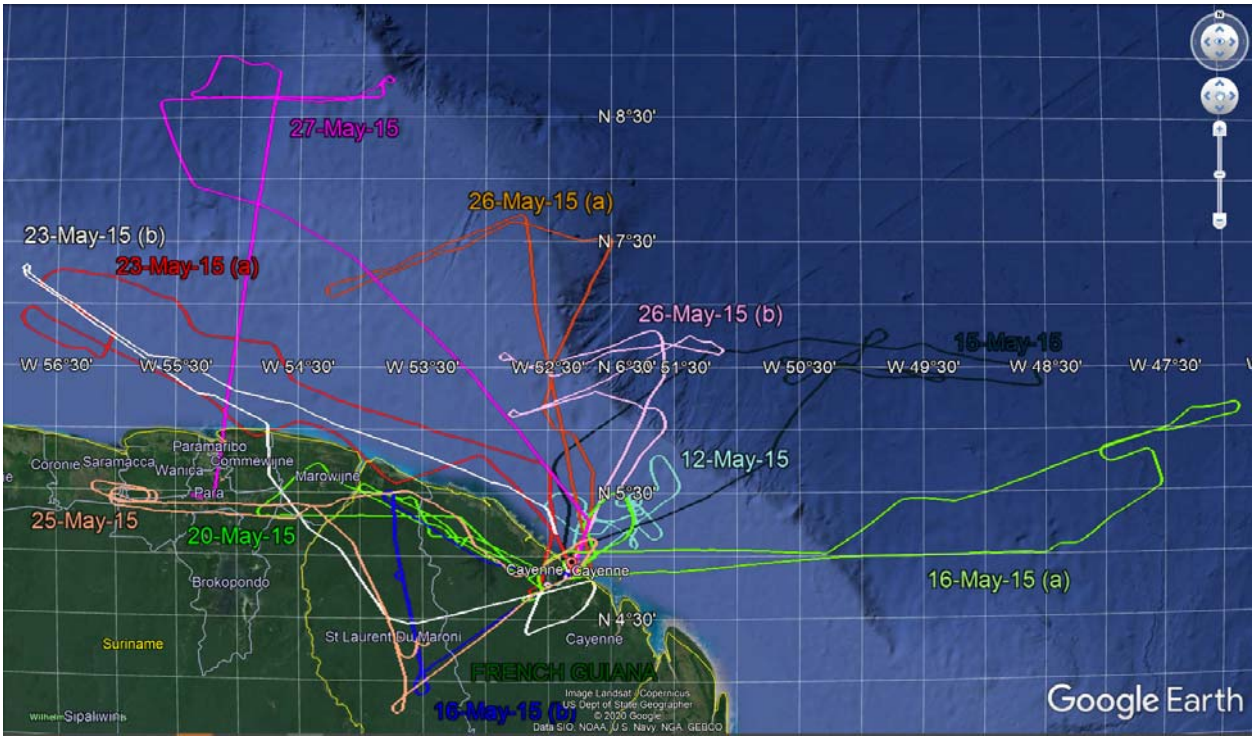

Figure 3. As in Fig. 1, but for ten NRC Convair 580 flights contributing to the Appendix D/P comparison during the HAIC-HIWC "Cayenne-15" flight campaign out of Cayenne, French Guiana from 5-29 May, 2015; 580 aircraft. Adapted from [9].

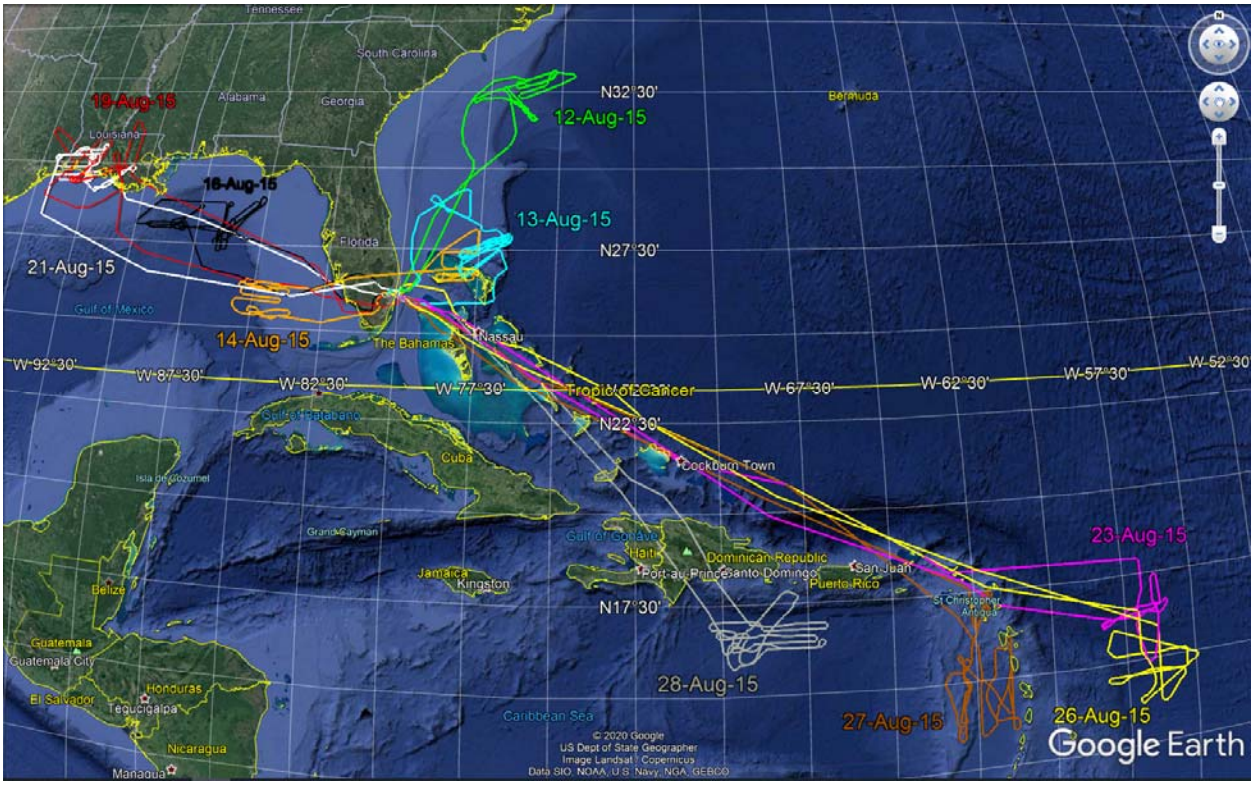

Figure 4. As in Fig. 1, but for ten DC-8 flights contributing to the Appendix D/P comparison during the NASA/FAA HIWC-RADAR I flight campaign out of Fort Lauderdale, Florida (Florida-15) from 12-28 Aug., 2015. Adapted from [31].

Figure 5. Photograph of two core instruments of the campaigns mounted under the wing of the Falcon-20: the isokinetic evaporator (IKP2) reference TWC instrument, and the DMT CDP-2.. The SEA Robust hot-wire TWC probe is also shown. The core SPEC-2D-S and DMT PIP probes are partially visible in the background under the other wing. See also Figs. 6-7.

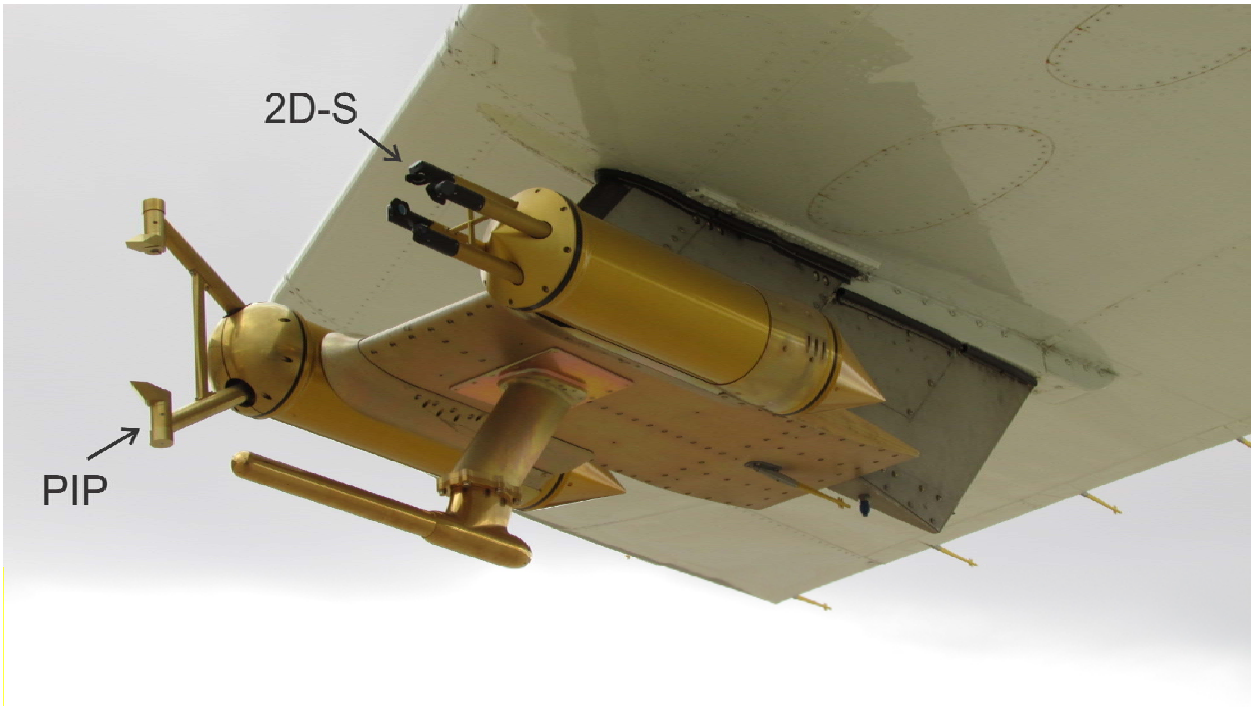

Figure 6. The DMT PIP and the SPEC 2D-S core instruments mounted under the wing of the DC-8 for the HIWC RADAR I (Florida-15) campaign. See also Figs. 5 and 7.

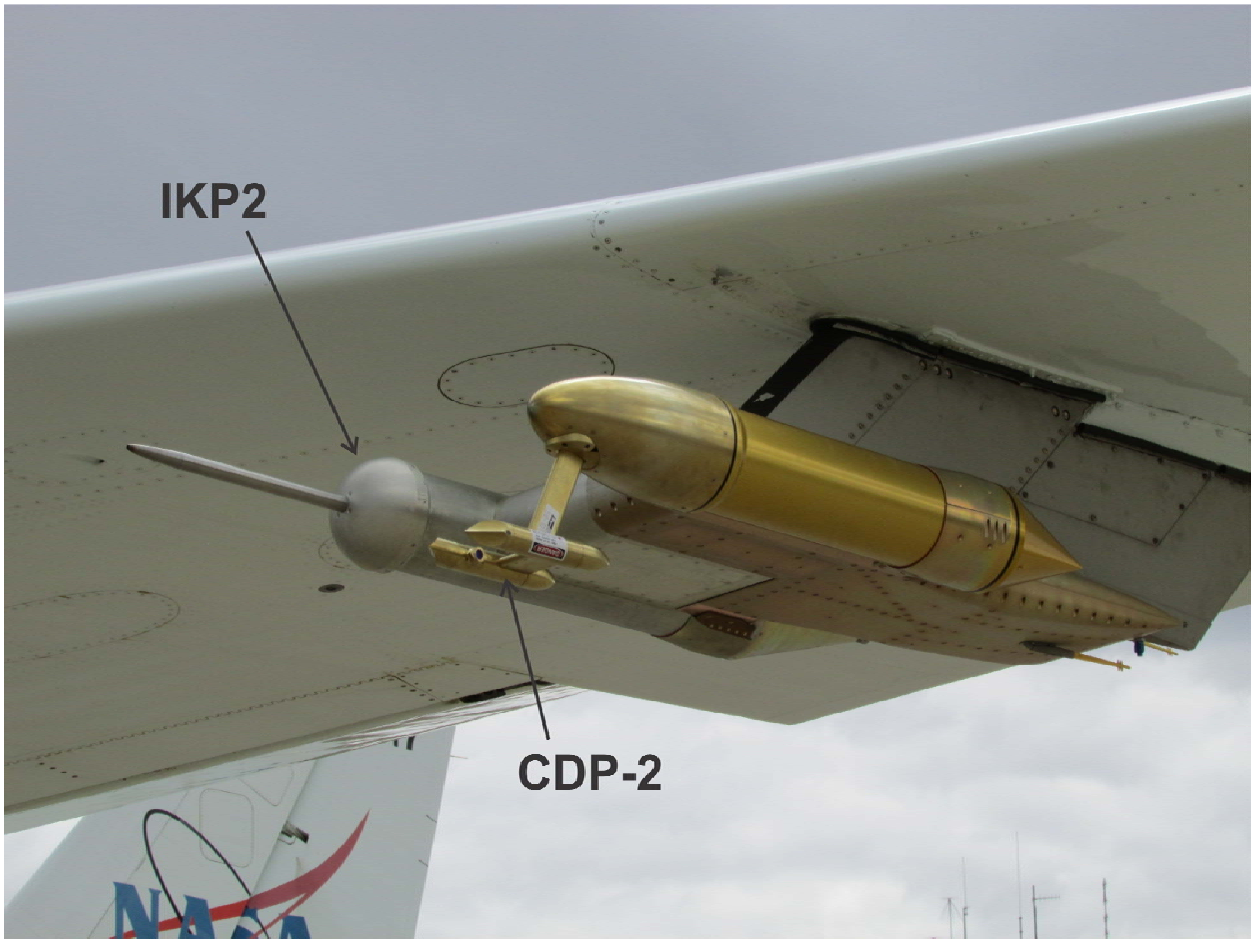

Figure 7. The IKP2 and the DMT CDP-2 core instruments mounted under the DC-8 port wing for the HIWC RADAR I (Florida-15) campaign. See also Figs. 5-6.

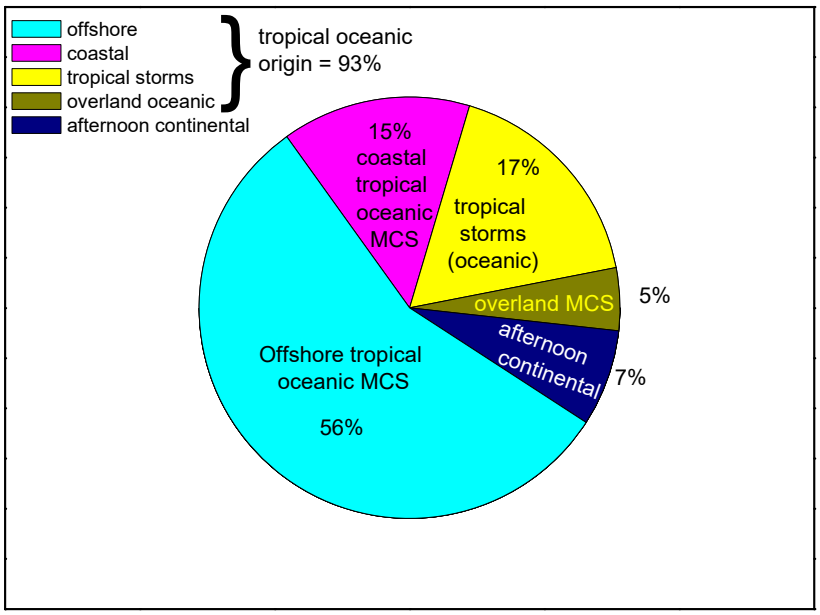

Figure 8. Percentage of in-cloud distance sampled from different cloud categories for the three datasets of the Darwin-14, Cayenne-15, and Florida-15 campaigns, from [9].

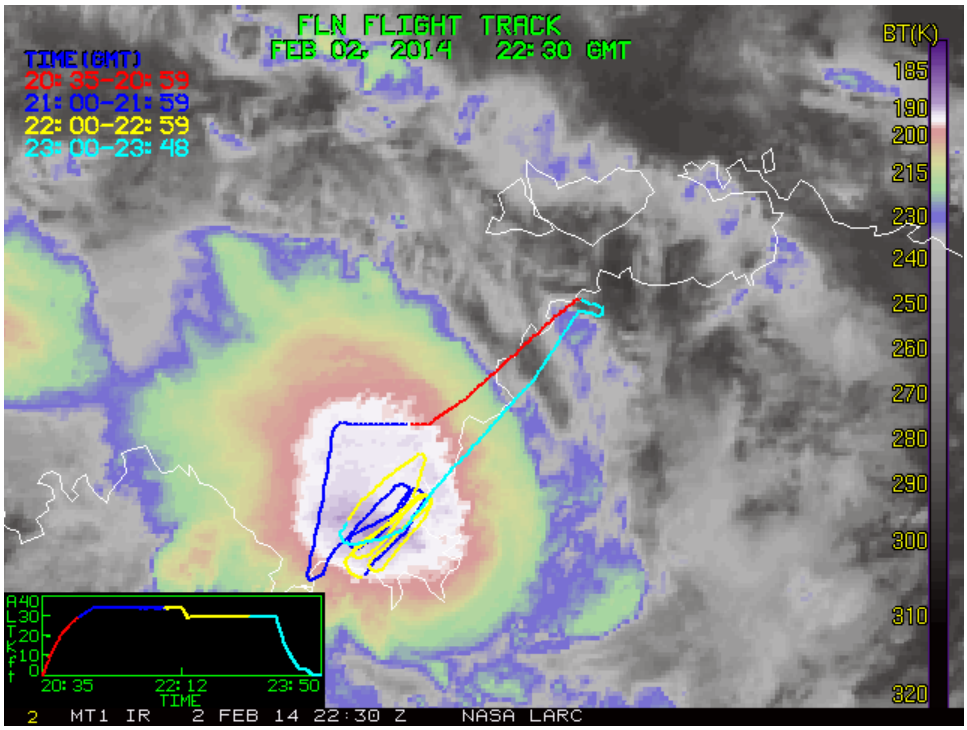

Figure 9. Flight track for Darwin-14 flight 12 on 2 Feb., 2014, in an un-named tropical storm, illustrating the survey pattern employed in sampling an oceanic cloud system, in this case without vigorous cells at altitude, from [9].Time histories of selected parameters for one cloud traverse for this case is given in Fig. 10.

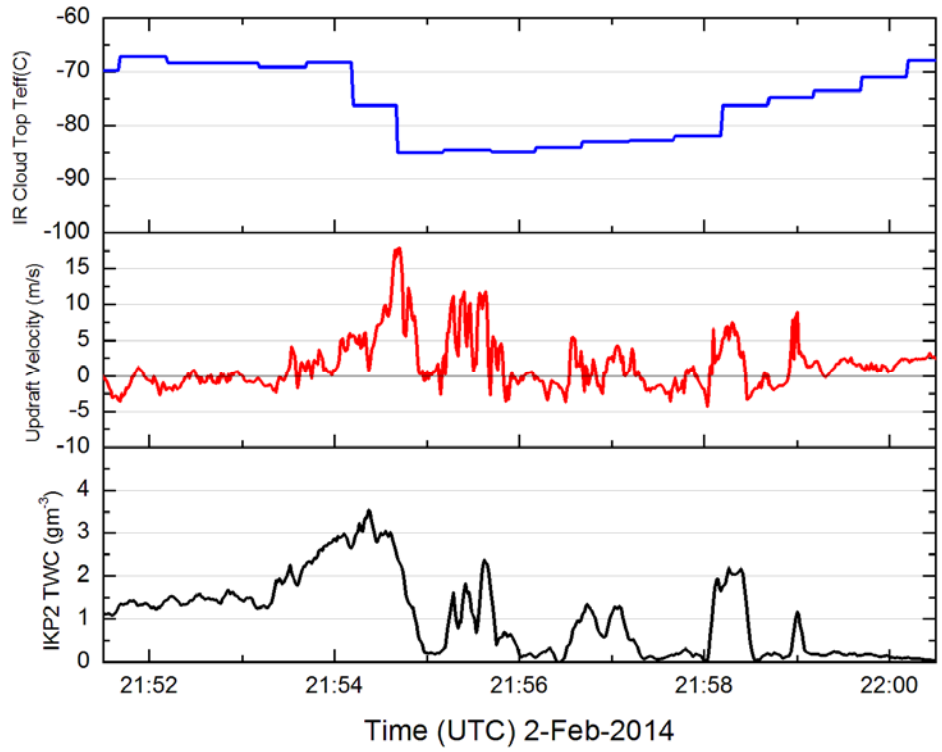

Figure 10. Sample time history of cloud parameters for a straight and level run from Darwin-14 Flight 12, from [9] (see also Fig. 9). Average in-cloud temperature and pressure altitude were -35.6 C and 33960 feet respectively.

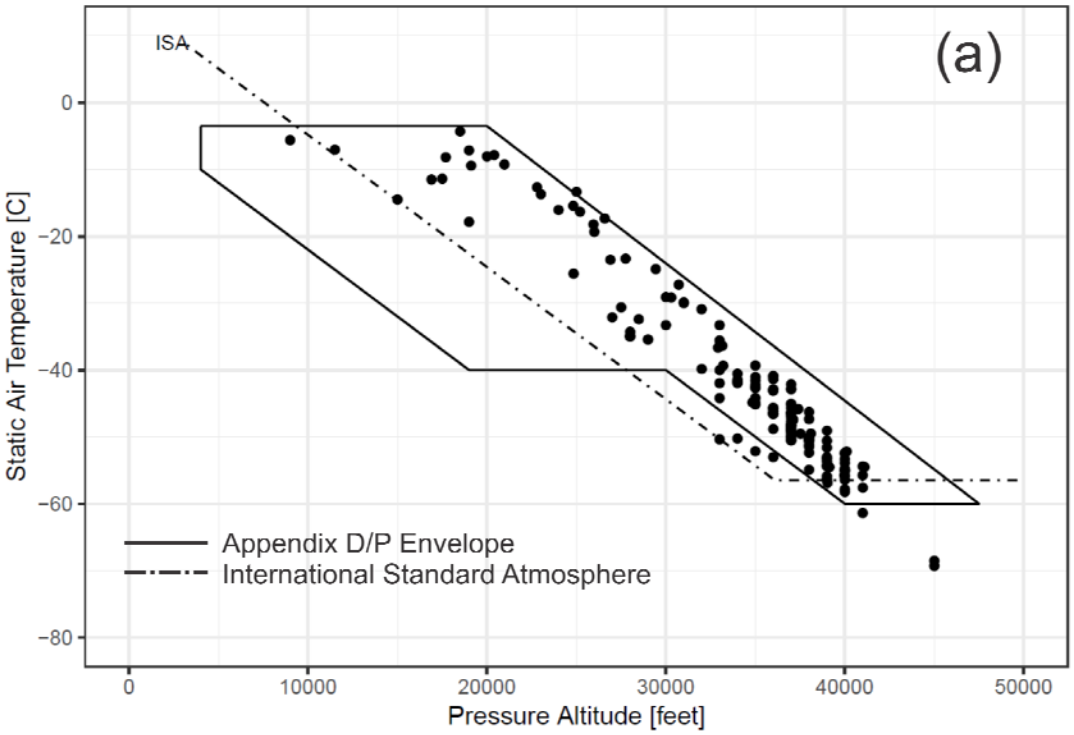
(a)
ISA
0
−20
−40
−60
−80
Static Air Temperature [C]
0
10000
20000
30000
40000
50000
Pressure Altitude [feet]
Appendix D/P Envelope
International Standard Atmosphere

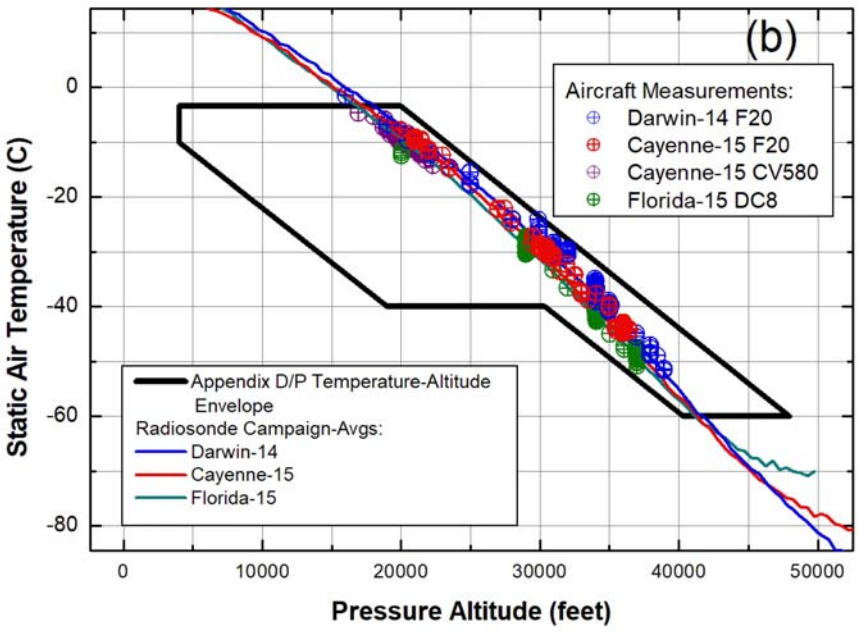

Figures 11 (a, b). (a) The inventory of 168 Boeing engine events from Apr. 1991 to Jan. 2019, for which static air temperature (SAT) and pressure altitude (feet) were available, adapted from [58]. The Appendix D/P temperature-altitude envelope and the International Standard Atmosphere are denoted by the solid and dash-dotted black lines respectively. (b) Temperature-altitude envelope data points for three flight campaigns, adapted from [9]. Data points are traverse averages, where a traverse usually represents a crossing of a cloud. Average radiosonde measurements closest to flights for each period are included as solid colored lines.

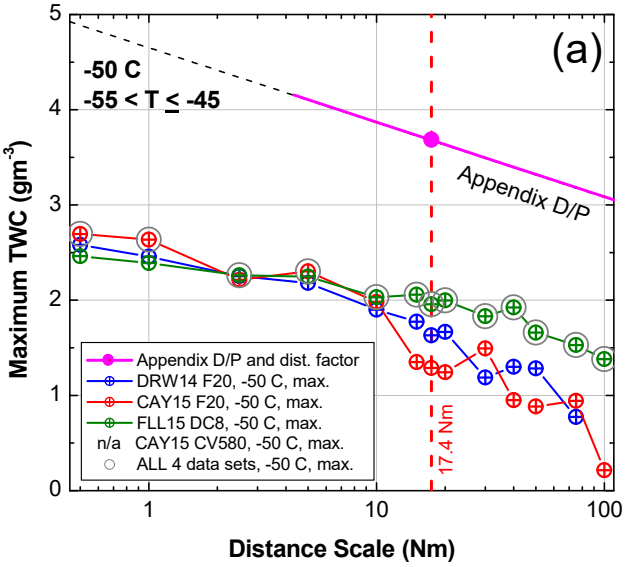
(a)
-50 C
-55 < T ≤ -45
Appendix D/P
17.4 Nm
Appendix D/P and dist. factor
DRW14 F20, -50 C, max.
CAY15 F20, -50 C, max.
FLL15 DC8, -50 C, max.
n/a CAY15 CV580, -50 C, max.
ALL 4 data sets, -50 C, max.
Maximum TWC (gm-3)
Distance Scale (Nm)
0
1
2
3
4
5
1
10
100

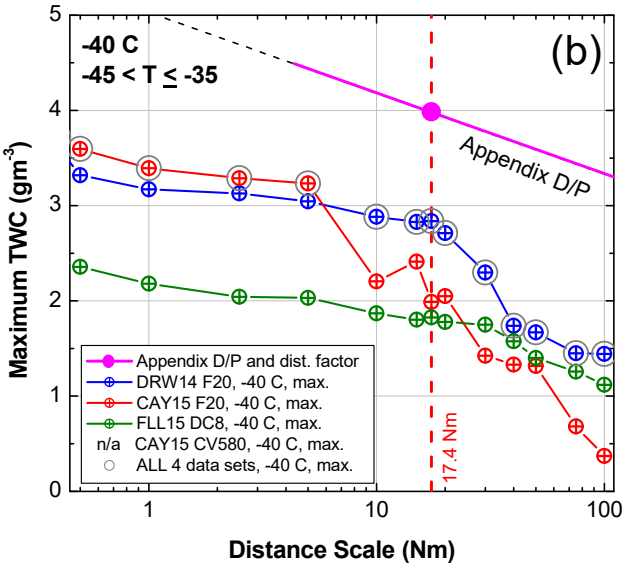
(b)
-40 C
-45 < T ≤ -35
Appendix D/P
17.4 Nm
Appendix D/P and dist. factor
DRW14 F20, -40 C, max.
CAY15 F20, -40 C, max.
FLL15 DC8, -40 C, max.
n/a CAY15 CV580, -40 C, max.
ALL 4 data sets, -40 C, max.
Maximum TWC (gm-3)
Distance Scale (Nm)
0
1
2
3
4
5
1
10
100

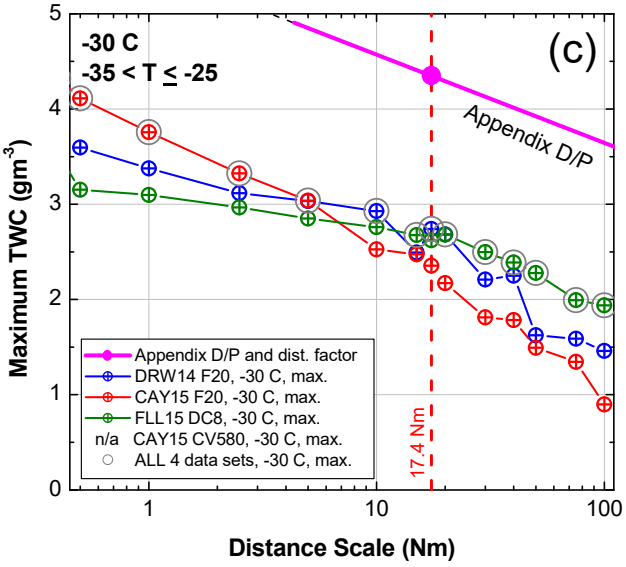

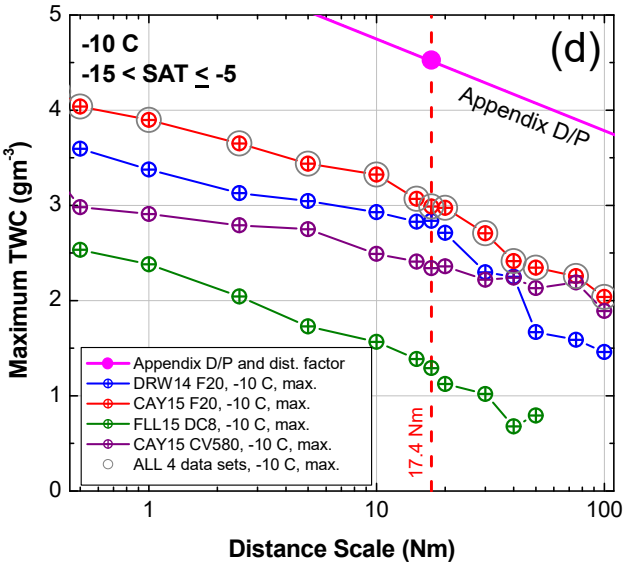

Figures 12 (a-d).Maximum TWC values as a function of distance scale as measured in Darwin-14 and Cayenne-15 on the Falcon-20 (DRW14 F20 and CAY15 F20), in Cayenne-15 on the Convair-580 (CAY15 CV580), and in Florida-15 on the DC-8 (FLL15 DC8) , adapted from [9] . Appendix D/P values are also shown. (a) -50 C, (b) -40 C, (c)-30 C, and (d) -10, all ±5 C.

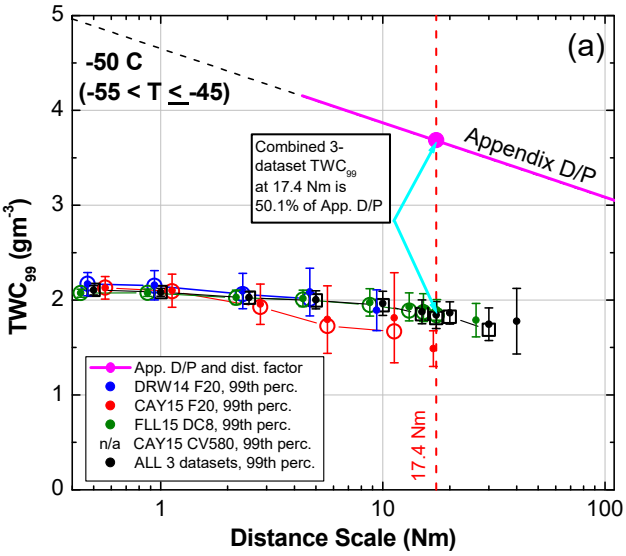
(a)
-50 C
(-55 < T ≤ -45)
Combined 3-dataset TWC99 at 17.4 Nm is 50.1% of App. D/P
Appendix D/P
App. D/P and dist. factor
DRW14 F20, 99th perc.
CAY15 F20, 99th perc.
FLL15 DC8, 99th perc.
n/a CAY15 CV580, 99th perc.
ALL 3 datasets, 99th perc.
17.4 Nm
TWC99 (gm-3)
Distance Scale (Nm)
0
1
2
3
4
5
1
10
100

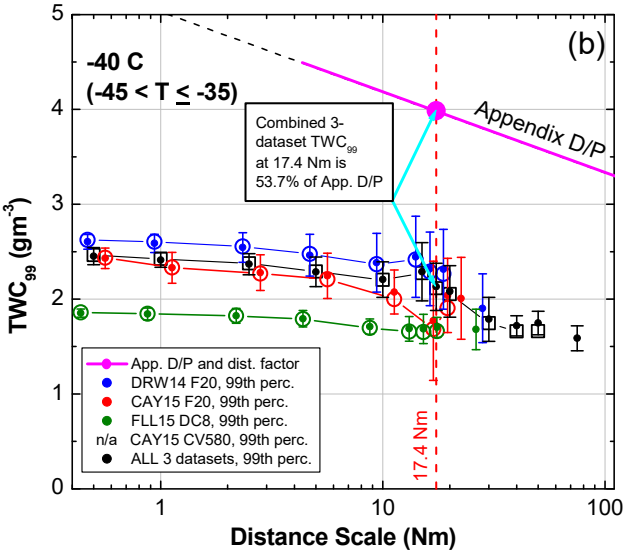
(b)
-40 C
(-45 < T ≤ -35)
Combined 3-dataset TWC99 at 17.4 Nm is 53.7% of App. D/P
Appendix D/P
App. D/P and dist. factor
DRW14 F20, 99th perc.
CAY15 F20, 99th perc.
FLL15 DC8, 99th perc.
n/a CAY15 CV580, 99th perc.
ALL 3 datasets, 99th perc.
17.4 Nm
TWC99 (gm-3)
Distance Scale (Nm)
0
1
2
3
4
5
1
10
100

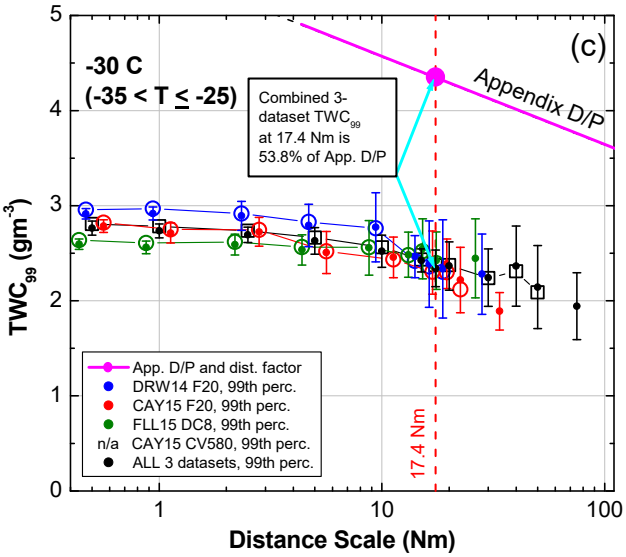

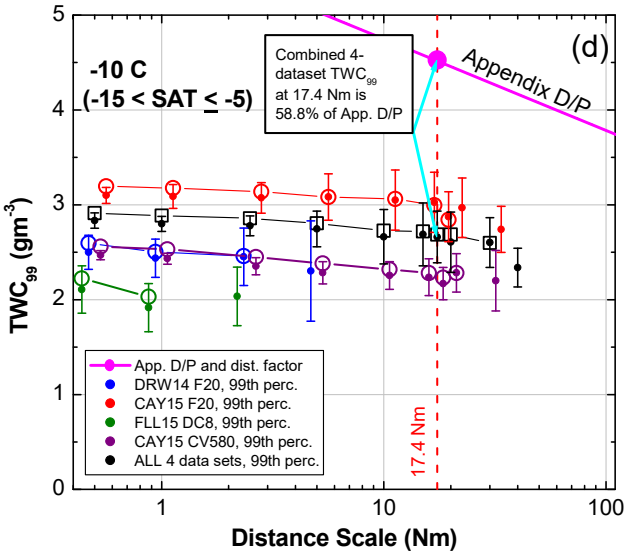

Figures 13(a-d). As in Figure 12, but for TWC_{99} rather than maximum TWC, versus distance, adapted from [9]. Final TWC_{99} values, incorporating a bias correction and uncertainty estimate for the combined effect of sampling statistics and the saturation assumption in the IKP2 TWC calculation, are shown as solid circles with ±2σ uncertainty bars. See text for further explanation. Symbol x-axis staggering is for better visualization, and the true distance scale is that of the combined datasets (black symbols).

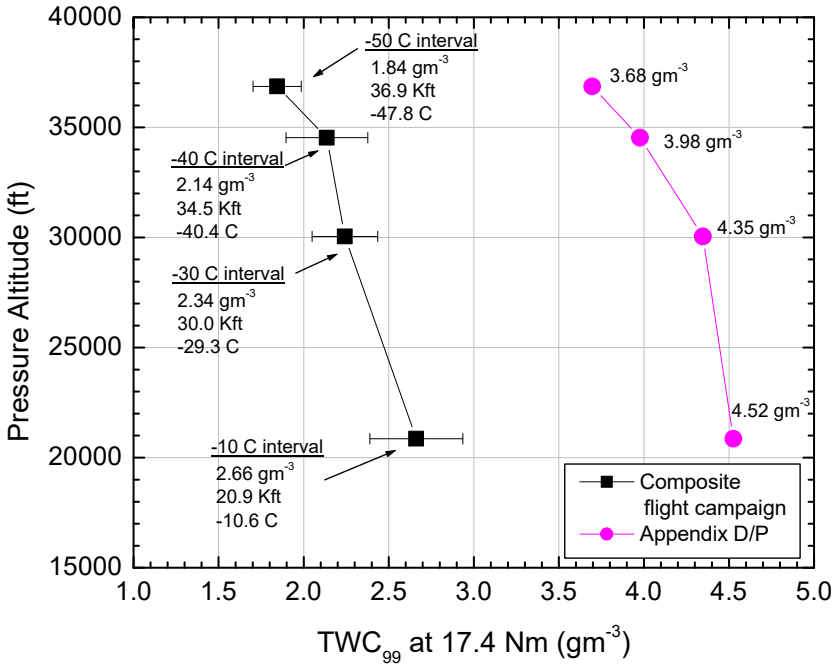

Figure 14. Flight campaign composite TWC_{99} values at 17.4 Nm versus pressure altitude, compared to Appendix D/P. For each temperature interval, campaign TWC_{99} values are included in text next to the black points, along with the average SAT and pressure altitude for the interval, and Appendix D/P values are included next to the magenta points.

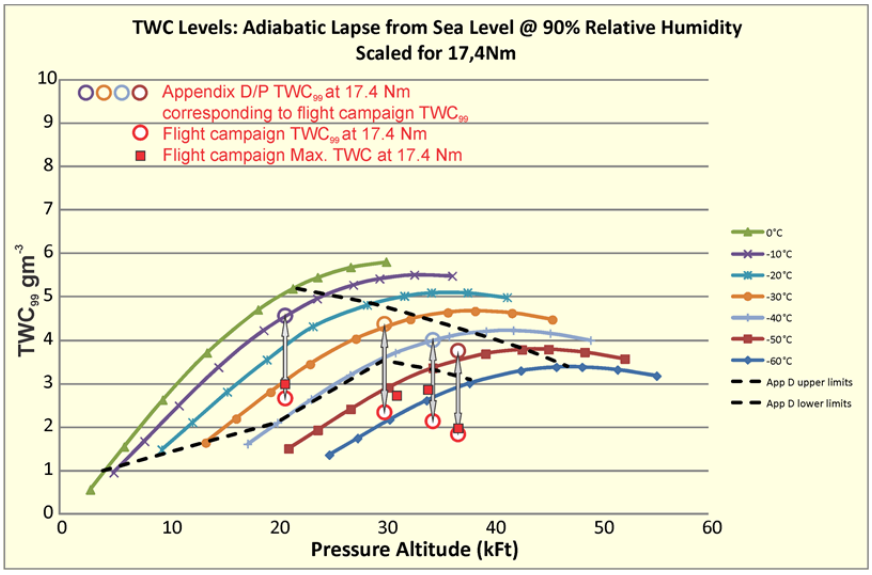

Figure 15. Summary of flight campaign TWC_{99} comparison overlaid on Appendix D/P TWC envelope. Flight campaign data are shown as open red circles at the average temperatures for the data points of the 4 intervals, with corresponding Appendix D/P

values directly above as denoted by the arrows. Red square symbols represent maximum TWC values in the intervals at 17.4 Nm. The Appendix D/P envelope limits are shown by the dotted black line, appropriate for Appendix D/P TWC_{99} values. Adapted from [3, 1, 2].

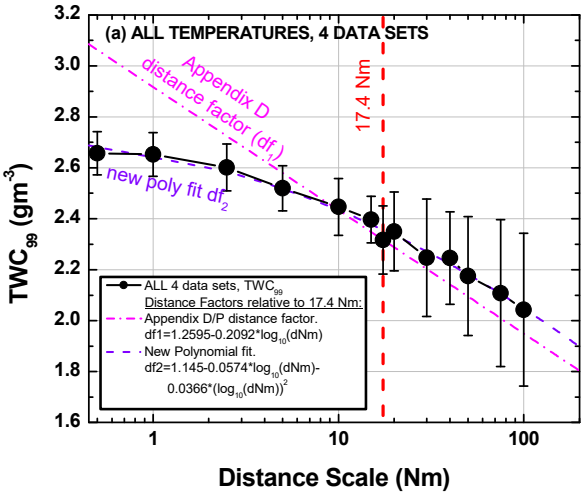

Figure 16. TWC_{99} versus distance for all datasets, all temperatures, with Appendix D/P distance factor df, adjusted to observed TWC_{99}, and new polynomial fit df_2 (see legend)to observations , adapted from [9].

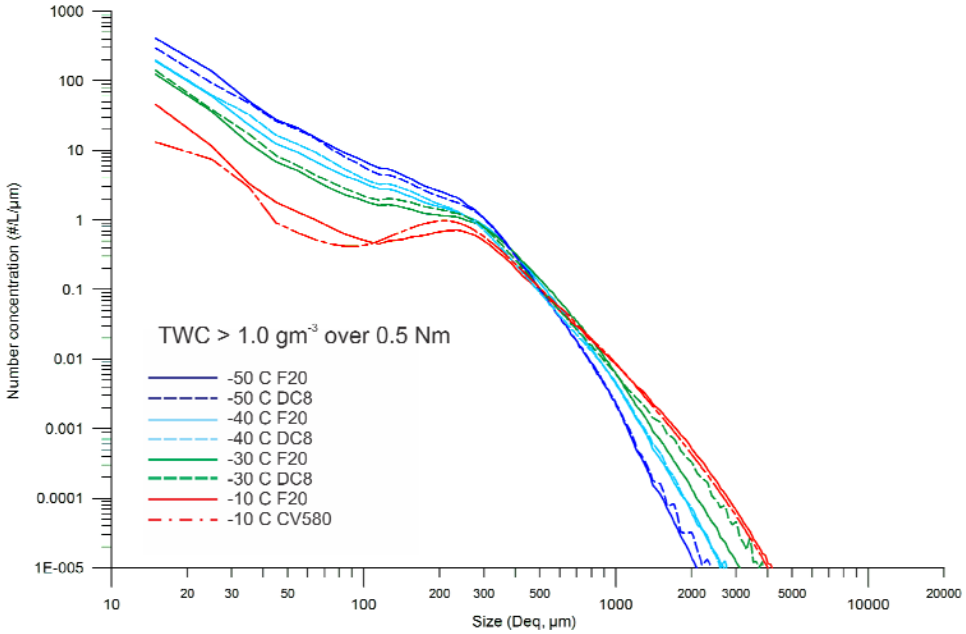

Figure 17. PSDs, or number concentration versus size, size defined as area equivalent diameter D_{eq}. Continuous and dashed lines are used for the Falcon-20 (F20) and DC-8 (DC8) datasets respectively. Dash-dot lines are used for the Convair 580 (CV580) dataset (-10 C only). Color denotes the temperature interval: -50° C level in dark blue, -40° C in light blue, -30° C in green and -10° C in red. There is insufficient data at -10° C for the DC-8. Adapted from [8] with Convair 580 added.

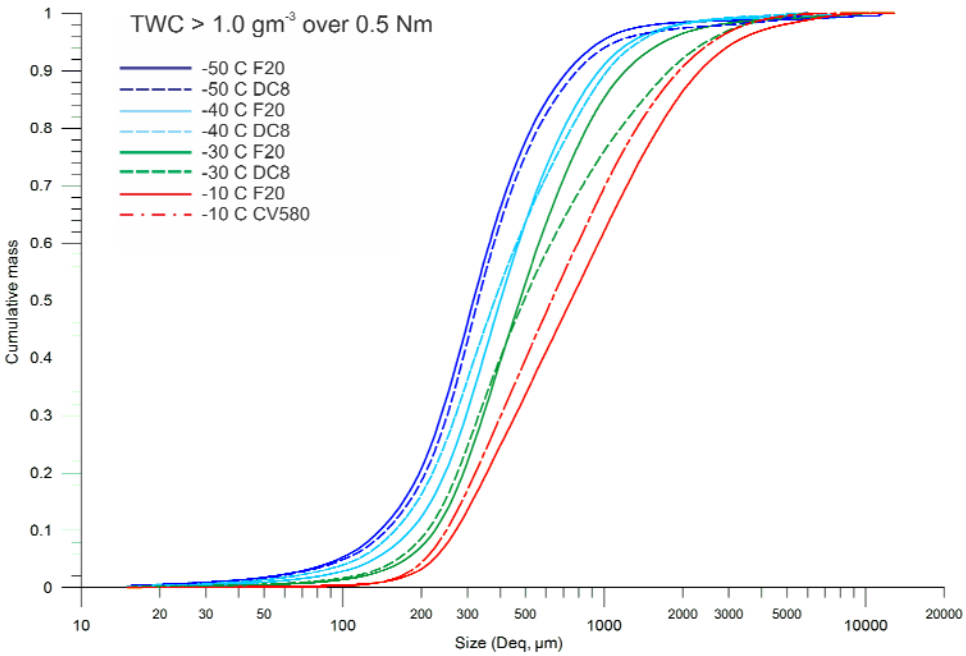

Figure 18. As in Figure 17, but converted to estimated mass, and represented here as cumulative mass distributions. Adapted from [8] with Convair 580 added.